Applied Ocean Research 116 (2021) 102888

Contents lists available at ScienceDirect

Applied Ocean Research

journal homepage: www.elsevier.com/locate/apor

Simulation of random wave overtopping by a WCSPH model

Corrado Altomare [a,*], Xavi Gironella [a], Alejandro J.C. Crespo [b]

[a] Maritime Engineering Laboratory, Universitat Politècnica de Catalunya - BarcelonaTech, 08034 Barcelona, Spain
[b] Environmental Physics Laboratory, Campus Sur, Universidade de Vigo, 32004 Ourense, Spain

ARTICLE INFO

Keywords:
Wave overtopping
Smoothed particle hydrodynamics
Dualsphysics
Sea dikes
Irregular waves

ABSTRACT

In this work the Weakly Compressible SPH-based (WCSPH) model DualSPHysics has been validated and applied to study the random wave overtopping of dike-promenade layout in shallow water conditions. Data from physical model tests carried out in a small-scale wave flume have been used for model validation. The results have been compared in terms of water surface elevation, mean discharges and individual overtopping volumes distribution. The selected geometrical layout is representative of the coastal area of Premià de Mar, in Catalonia (Spain). This stretch of the coast presents both railways and a bike path very close to the shore and therefore exposed to possible sea storms. For the first time an SPH-based model has been employed to reproduce long-lasting wave overtopping tests, made of time series of 1000 irregular waves, which are representative of real sea states. The density diffusion scheme and the modified Dynamic Boundary Conditions have been applied in the present simulations. By employing standard setup for SPH modelling of wave-structure interaction problems of a very long duration, stable simulations and accurate results have been attained.

1. Introduction

Wave overtopping is the major cause of wave flooding in urbanised coastal areas and therefore is still considered a key aspect for any coastal engineering design. Overtopping is stochastic, dynamic, temporally variable phenomenon, characterized by episodic individual events during an entire sea storm duration. Statistical methods are not able to represent temporally variable overtopping flows. Instead, numerical modelling is an attractive tool for studying overtopping flows: if properly validated, it may be adapted for any desired structure, geometry and wave condition. Moreover, numerical models do not suffer from scale effects and can provide information on physical quantities that could be difficult to measure in scaled models or in prototypes. Despite there is already an extensive literature on wave overtopping assessment (EurOtop, 2018), wave overtopping is currently considered a significant deficiency in flood modelling of urban areas (Gallien et al., 2014).

Phase-average wave models (Booij et al., 1996) can be employed to propagate waves, however they do not resolve the stochastic uncertainty of the random phasing (Williams et al., 2014) and the relative wave fields when computing overtopping metrics (e.g., standing waves, bores, freak/rogue waves cannot be properly resolved). A variety of phase-resolving methods have been developed and applied to wave overtopping: Boussinesq-type models (Lynett, 2006), Nonlinear Shallow Water (NLSW) equation-based models (Zijlema et al., 2011), Navier-Stokes (NS) equations models (Gruwez et al., 2020a; Lashley et al., 2020). In particular, NS equations resolve complex hydrodynamics such as wave breaking and wave-structure interaction phenomena (Losada et al., 2008) directly. In general, there are two main methodological frameworks to solve NS equations: mesh-based and mesh-less approaches. Mesh-based models, also called Eulerian models, discretize the domain using some type of mesh to analyse the variables of interest at fixed nodes by solving the governing equations. To do so, numerical methodologies as, for example, finite volume techniques are employed. These methods proved to be robust and accurate over the years to study complex flows (De Finis et al., 2020). However, they are characterised by expensive mesh generation and have severe technical challenges associated with implementing conservative multi-phase schemes or with large deformations that lead to mesh deformation.

On the contrary, mesh-less or Lagrangian methods allow overcoming part of the drawbacks that characterise the mesh-based schemes. Methods such as Smoothed Particle Hydrodynamics (SPH) (Violeau, 2012) have been growing and gaining more and more attention within the scientific community because they do not require special surface tracking and are inherently capable to capture non-linearities. Despite solvers based on Eulerian and Lagrangian methods have proven successful for modelling wave overtopping phenomena, they still require

* Corresponding author.
E-mail addresses: corrado.altomare@upc.edu (C. Altomare), xavi.gironella@upc.edu (X. Gironella), alexbexe@uvigo.es (A.J.C. Crespo).

https://doi.org/10.1016/j.apor.2021.102888
Received 10 May 2021; Received in revised form 6 September 2021; Accepted 14 September 2021
Available online 25 September 2021
0141-1187/© 2021 The Authors. Published by Elsevier Ltd. This is an open access article under the CC BY-NC-ND license (http://creativecommons.org/licenses/by-nc-nd/4.0/).

Fig. 1. View of a stretch of the coast area in Premià de Mar: the bike line and railway run at a few metre from the sea.

huge computational efforts and are unlikely to be applied for field scale or long wave train (i.e., 1000 waves) simulations. To cope with high computational costs, SPH method allows nowadays the use of graphics processing units (GPU) to accelerate the computations, as for example implemented in DualSPHysics solver (Domínguez et al., 2021).

Latest advances in SPH have proven the accuracy of the method when applied to coastal engineering problems (González-Cao et al., 2019; Gotoh and Khayyer, 2018; Khayyer et al., 2008; St-Germain et al., 2014; Wen et al., 2018, 2016; You et al., 2021). However, for wave overtopping simulation there is no exhaustive literature, or the applications are limited to simple and regular waves trains or time series with short duration.

Shao (2006) employed the incompressible approach of SPH to simulate regular and random wave overtopping, but duration of random wave trains was relative short, about 180 s, corresponding to only 30–50 waves per time series. Akbari (2017) implemented an improved treatment of the viscosity of surface particles at the boundaries in order to reduce the numerical error when calculating the flow acceleration at the boundary due to the truncation of kernel function and contribution of fewer particles in solving the governing equations. Akbari (2017) presented very detailed simulations capable to resolve the characteristics of the individual overtopping flow, however the simulation of real wave sea states is not performed and very short time series of individual or regular waves were studied. Mokos et al. (2020) employed the GPU-SPH single phase code to simulate regular wave overtopping on complex geometries. A quasi-3D modelling is presented by those authors, where the boundaries are treated based on the Dynamic Boundary Condition (DBC) method (Crespo et al., 2007). The validation, however, does not involve time series of overtopping volumes, not available from the employed experimental campaign. Gruwez et al. (2020a) carried out an inter-model comparison between OpenFoam, SWASH and DualSPHysics models to study bichromatic wave transformations over a steep-sloped dike with a mildly-sloped and very shallow foreshore. Overall the results showed that SPH-based methods have attained similar model performance of mesh-based approaches at even lower computational cost. However, the lack of multi-resolution (adaptivity) is still a bottleneck of the SPH simulations (Vacondio et al., 2021). The work carried out by the authors employed a very fine resolution in order to catch the complex hydrodynamics of the individual flows overtopping the dike and hitting the walls, but for very short time series. Dang et al. (2021) used DualSPHysics to study wave-induced forces and overtopping for regular waves only. While the authors provided a rigorous model comparison with analytical solutions only for forces, they carried out some overtopping modelling for different layouts but without any validation.

The goal of the present work is to demonstrate that SPH-based solvers have attained a level of maturity for which they can be employed to reproduce long-lasting wave overtopping tests, made of time series of 1000 irregular waves, which are representative of real sea states, keeping a trade-off between model accuracy and computational cost. Although it has been recently demonstrated that individual overtopping flow properties, such as flow velocities and depth, are of extreme importance in order to assess hazards for pedestrians and vehicles standing or right behind the costal defenses (Altomare et al., 2020; Mares-Nasarre et al., 2019; Sandoval and Bruce, 2017), generally, the design of any coastal defence worldwide is still based on the assessment of mean discharge values and individual maximum overtopping volumes, two quantities largely employed to establish safety and security thresholds for structural stability, vehicles (including small and large boats and ships) properties and people safety. Focus of this work is therefore to properly model time series of overtopping volumes, from which maximum individual overtopping events can be identified and mean discharges can be derived. To resolve the hydrodynamics of each individual overtopping flow would require very fine model resolutions or the use of sophisticated coupling techniques, which is not the aim of this work. Instead, DualSPHysics code is here proposed as a tool for coastal engineering in practice to provide preliminary insight into the wave overtopping of sea dikes, generating several overtopping scenarios in a reasonable computation time.

2. Experimental campaign

The experimental campaign was carried out in the small-scale wave and current flume facility CIEMito at Maritime Engineering Laboratory (LIM) of Universitat Politècnica de Catalunya - BarcelonaTech (UPC), in Spain (Altomare, 2021). The experiments focused on the measurements of wave overtopping on smooth sea dikes with shallow foreshores and wide crest promenade. The experimental work aims to establish the correlation between overtopping volumes and discharges and the corresponding overtopping flow velocities and overtopping flow depth. The physical model mimicked an urbanised stretch of a town along the Catalan coast (Premià de Mar), approximately 25 km northeast of Barcelona, where a bike path and a railway run along the coastline, exposed to significant overtopping events every stormy season (Fig. 1). The effect of the rubble mound has not been taken into account: instead, a smooth sloping dike has been modelled (Altomare et al., 2020).

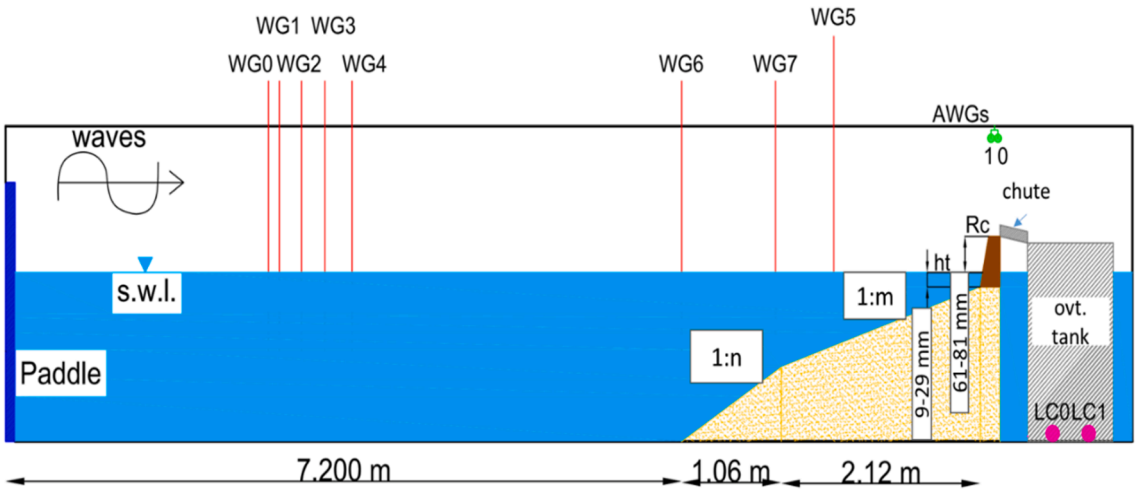

Fig. 2. CIEMito wave flume - drawing of the longitudinal section (distorted). Dimensions are in model scale (source: Altomare et al., 2020).

Table 1
Location from paddle of resistive wave gauges (in meters).

Sensor	WG0	WG1	WG2	WG3	WG4	WG6	WG7	WG5
x ($m = 15$)	2.8	2.96	3.15	3.40	3.69	7.20	8.20	8.82
x ($m = 30$)	2.8	2.96	3.15	3.40	3.69	7.20	8.26	8.82

Table 2
Main characteristics of the selected test cases for numerical model validation (expressed in model scale, 1:50).

Case #	Foreshore slope (1:n)	$H_{m0,o}$ [m]	T_p (s)	h_{deep} [m]	h_{toe} [m]
1	30	0.110	1.40	0.310	0.029
2	15	0.100	1.79	0.300	0.019
3	30	0.090	1.40	0.305	0.024
4	15	0.090	1.50	0.290	0.009
5	15	0.100	1.79	0.300	0.019
6	15	0.088	1.74	0.300	0.019
7	30	0.085	1.69	0.310	0.029
8	15	0.088	1.74	0.300	0.019
9	30	0.100	1.60	0.305	0.024
10	30	0.100	1.60	0.300	0.019
11	30	0.090	1.60	0.310	0.029
12	30	0.090	1.70	0.305	0.024
13	15	0.100	1.5	0.290	0.009
14	15	0.085	1.69	0.300	0.019
15	15	0.090	1.700	0.310	0.029
16	15	0.088	1.74	0.300	0.019
17	15	0.085	1.69	0.300	0.019
18	15	0.085	1.69	0.300	0.019
19	15	0.085	1.69	0.300	0.019
20	30	0.100	1.40	0.305	0.024

2.1. Experimental setup

The CIEMito wave flume is 17 m long, 0.37 m wide and 0.56 m high. A maximum water depth of 0.36 m is allowed. The wave generation system is a piston-type board, made of a vertical panel whose motion is provided by a linear actuator allowing a maximum stroke of 1 m with a response speed of 1.6 m/s. The paddle moved backwards and forwards horizontally. Wave generation software was developed at LIM/UPC and allows the generation of both regular and irregular waves with a maximum wave height of 0.28 m and a maximum peak period of 1.7 s.

The employed model-scale was 1:50, according to Froude's similarity law. A sketch of the model layout is proposed in Fig. 2 (dimensions are in model scale). The model consists of a 1:n transition slope followed by a 1:m foreshore slope, where n is equal to 8 for $m = 15$ and 5 for $m = 30$, respectively. A 1:1 smooth dike made of polymethyl methacrylate was mounted at the end of the foreshore. Dike height was 0.09 m. Different widths for the promenade (i.e. crest berm) were modelled, namely 0.12 and 0.24 m, to be representative of the different stretches along the coastline. For numerical model validation purposes, only tests with promenade of 0.24 m are considered. Irregular wave tests, employing a JONSWAP spectrum with enhancement factor equal to 3.3, were performed. Each test consisted in approximately 1000 waves. In total 420 tests were conducted, 20 of which have been selected for the present numerical model validation.

The experimental tests carried out are aimed to measure the following parameters: free surface water elevations, η [m]; cumulative Volume, V_{tot} [m^3/m]; mean discharge, q [l/s/m], obtained as $\frac{V_{tot}}{T_p N_w}$, where T_p is the wave peak period and N_w is the number of wave forming the wave train; maximum overtopping volume,V_{max} [l/m]; velocity of maximum overtopping volume, u [m/s]; thickness of maximum overtopping volume, λ[m]. Considering the chosen numerical model setup and model resolution, only volumes and discharges have been analysed and used for comparison in the present work, as discussed later.

Water surface elevation was measured by means of 8 resistive Wave gauges (WG0, …, WG7). They essentially consist of a pair of parallel stainless-steel electrodes connected to a voltage generator. The overtopping collection system was made of a 9.2 cm large chute which redirected the overtopping flows and brought it inside a metallic water tank of 27 l capacity. Under the tank two beam type load cells (model Z6FC3, rated capacity = 50 kg) were installed in order to measure the cumulated water weight. The cumulated volume was obtained by dividing weight by water density. Water surface elevation and overtopping volumes were acquired using a sampling frequency of 80 Hz and 20 Hz, respectively. Location of the wave gauges is reported in Table 1.

2.2. Selected experimental tests

Twenty cases have been selected for numerical model validation. See Table 2. Foreshore slopes of both 1:15 and 1:30 have been considered, since the wave breaking process is expected to be different in the two cases, i.e. heavier breaking for the gentler slope. Spectral wave height and peak period refer to the target conditions at wave generation. The water depth at wave generation, h_{deep}, and at the dike toe, h_{toe}, are reported. All cases correspond to very and extremely shallow water cases (Hofland et al., 2017).

The measured mean discharge values and maximum individual overtopping volumes are reported in Table 3. All values will be reported in prototype scale hereafter, to allow the classification with respect to tolerable overtopping design criteria as proposed in literature (EurOtop,

Table 3
Measured overtopping discharges (q), maximum individual overtopping volumes (V_{max}), overtopping flow depth values (λ), (expressed in prototype dimension) and wave steepness (s_0) for each test case.

Case #	s_0	q (l/s/m)	V_{max} (l/m)	λ (m)
1	0.029	17.43	2662.16	0.24
2	0.020	16.48	8701.91	NaN
3	0.023	1.06	1125.63	NaN
4	0.022	0.85	1774.74	NaN
5	0.021	17.68	8640.39	1.25
6	0.019	13.68	8898.89	1.50
7	0.019	8.59	3080.53	0.22
8	0.019	10.92	5260.02	0.55
9	0.023	6.97	2685.51	NaN
10	0.027	2.72	1643.91	0.16
11	0.023	12.02	3713.9	0.21
12	0.018	3.32	2950.79	0.38
13	0.026	1.91	1899.48	0.28
14	0.019	7.25	3827.24	0.50
15	0.022	43.73	8957.31	NaN
16	0.019	10.15	6256.68	0.37
17	0.020	9.33	4896.37	0.73
18	0.020	7.18	4437.35	0.70
19	0.015	5.41	4447.03	0.37
20	0.018	4.63	2595.95	0.38

Table 4
Classification of the relative refined index of agreement d_r and corresponding rating.

d_r classification [-]	Rating
0.90 - 1.00	*Excellent*
0.80 - 0.90	*Very Good*
0.70 - 0.80	*Good*
0.50 - 0.70	*Reasonable/Fair*
0.30 - 0.50	*Poor*
(−1.00) - 0.30	*Bad*

2018). Values of the overtopping flow depth, λ, and the deepwater wave steepness are also reported in Table 3, being the latter one ranging between 0.015 and 0.029. The flow depth was not measured for all tests; for those where this measurement is not available, NaN is reported in the table. Besides, the reader must consider the values of λ as characteristic values for each tests, which means that they are not maximum values measured during each experimental test, but the values associated to the maximum individual overtopping volume.

2.3. Scale effects

Surface waves and wave-structure interaction phenomena are governed by gravity forces. Model scale tests hence require to apply the Froude's similarity law, meaning that other forces related to friction, surface tension and viscosity are neglected, however, they might have an influence on the modelled phenomena if relative small model scales are employed. Working at 1:50 model scale requires a careful assessment of possible scale effects (Heller, 2011). The influence of viscous forces and surface tension was analysed for the present experimental campaign in Altomare et al. (2020), in accordance with what was reported in EurOtop (2018) and Schüttrumpf and Oumeraci (2005). The effect of friction is neglected for the very smooth materials employed to build the model.

The Reynolds and Weber numbers for wave overtopping (R_{eq} and W_{eq}) were calculated, ranging between 100 and 1200 and 6 and 180, respectively. The results were compared versus the proposed critical limits, namely $R_{eq} > 10^3$ and $W_{eq} > 10$. Where the calculated values fell behind the critical ones, a correction to the mean measured discharge values was applied (Schüttrumpf and Oumeraci, 2005) and omitted here for the sake of brevity. The correction calculated with Schüttrumpf and Oumeraci (2005) method ranged between 1 and 1.79.

3. Numerical model

3.1. DualSPHysics model

The present study uses the open-source solver DualSPHysics v5.0 (http://dual.sphysics.org/) based on Weakly Compressible SPH (Domínguez et al., 2021). DualSPHysics is written in two languages, namely *C++* and CUDA, and optimised to use the parallel processing power of either CPUs and/or GPUs. In the DualSPHysics, a quintic Wendland kernel (Wendland, 1995) with a compact support of radius $2h_{SPH}$ is applied. The smoothing length, h_{SPH}, is defined as function of the initial particle distance, *dp*, used to create the initial condition.

Physical quantities are computed for a given particle *a* considering

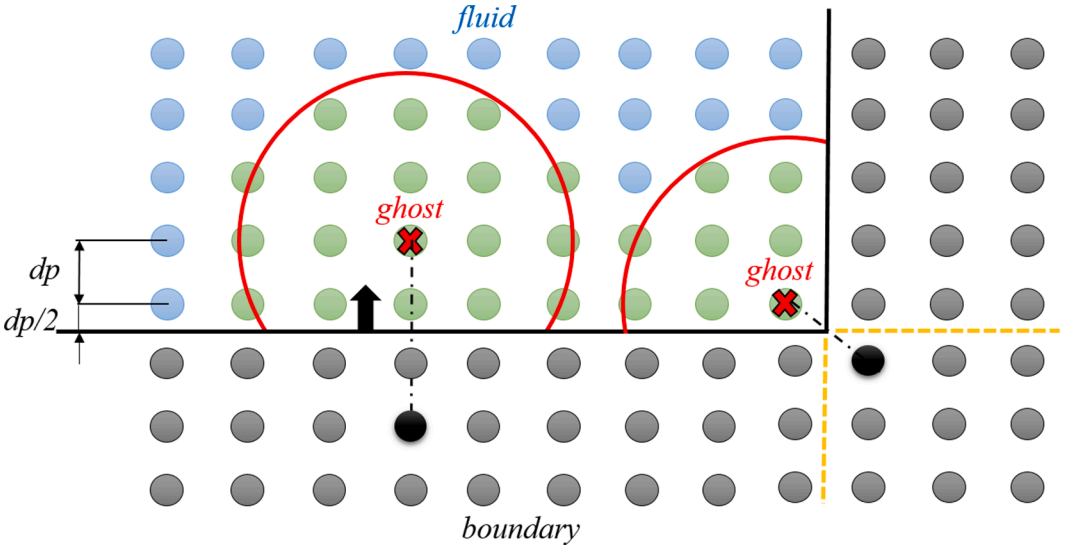

Fig. 3. Generation of ghost nodes (red crosses) by mirroring the boundary particles and definition of the kernel radius, for a flat surface and corner (boundary particles are coloured by grey, those selected as example for the mirroring are coloured by black; fluid particles are coloured by blue, those included in kernel summation of ghost nodes are coloured by green). The boundary interface is represented by the black solid line. (For interpretation of the references to colour in this figure legend, the reader is referred to the web version of this article.)

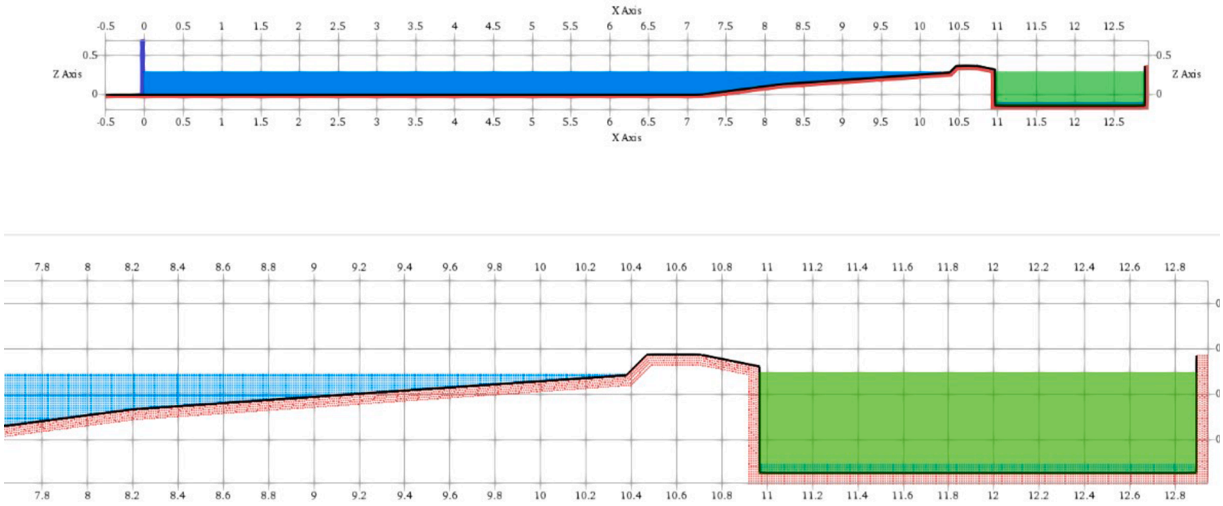

Fig. 4. Numerical layout corresponding to 1:15 foreshore slope: the fluid particles are depicted in blue colour, while the boundary layer is in red. The solid black line corresponds to the mDBC interface, while the shadowed green area indicates the area employed by FlowTool to detected the overtopping volumes. (For interpretation of the references to colour in this figure legend, the reader is referred to the web version of this article.)

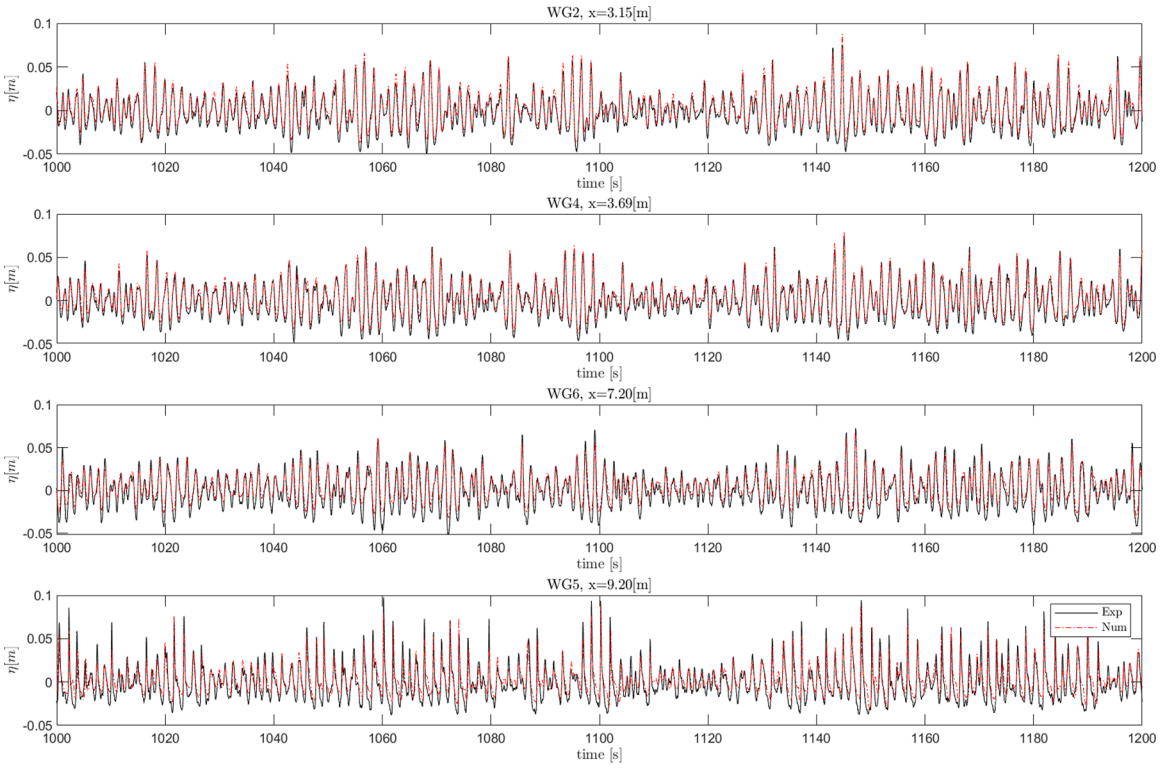

Fig. 5. Comparison of the h time series at WG2, WG4, WG7 and WG5 location for test #17 for a 200 s time window (results shown in model scale, 1:50).

the interaction with neighbouring particles b to solve the momentum and continuity equations, that can be written in the discrete SPH formalism as

$$\frac{\mathrm{d}\boldsymbol{v}_a}{\mathrm{d}t} = -\sum_b m_b \left(\frac{p_b + p_a}{\rho_b \cdot \rho_a} + \Pi_{ab} \right) \nabla_a W_{ab} + \boldsymbol{g} \tag{1}$$

$$\frac{\mathrm{d}\rho_a}{\mathrm{d}t} = \sum_b m_b \boldsymbol{v}_{ab} \nabla_a W_{ab} + D \tag{2}$$

$$\text{beging } D = 2\delta h_{SPH} c \sum_b (\rho_b - \rho_a) \frac{\boldsymbol{r}_{ab} \nabla_a W_{ab}}{\boldsymbol{r}_{ab}^2} \frac{m_b}{\rho_b} \tag{3}$$

where t is the time, $\boldsymbol{r}$ is the position, $\boldsymbol{v}$ is the velocity, p is the pressure, ρ is the density, m is the mass, c is the numerical speed of sound, and $\boldsymbol{g}$ is the gravitational acceleration. The artificial viscosity (Π_{ab}) is used, tuned with parameter α, preventing particles from interpenetrating providing numerical stability for free-surface flows (Monaghan, 2005). Besides, employing the artificial viscosity scheme has been shown to exhibit interesting features related to the turbulence field under breaking waves (Lowe et al., 2019).

The artificial viscosity term can be expressed as follows (Monaghan, 1992):

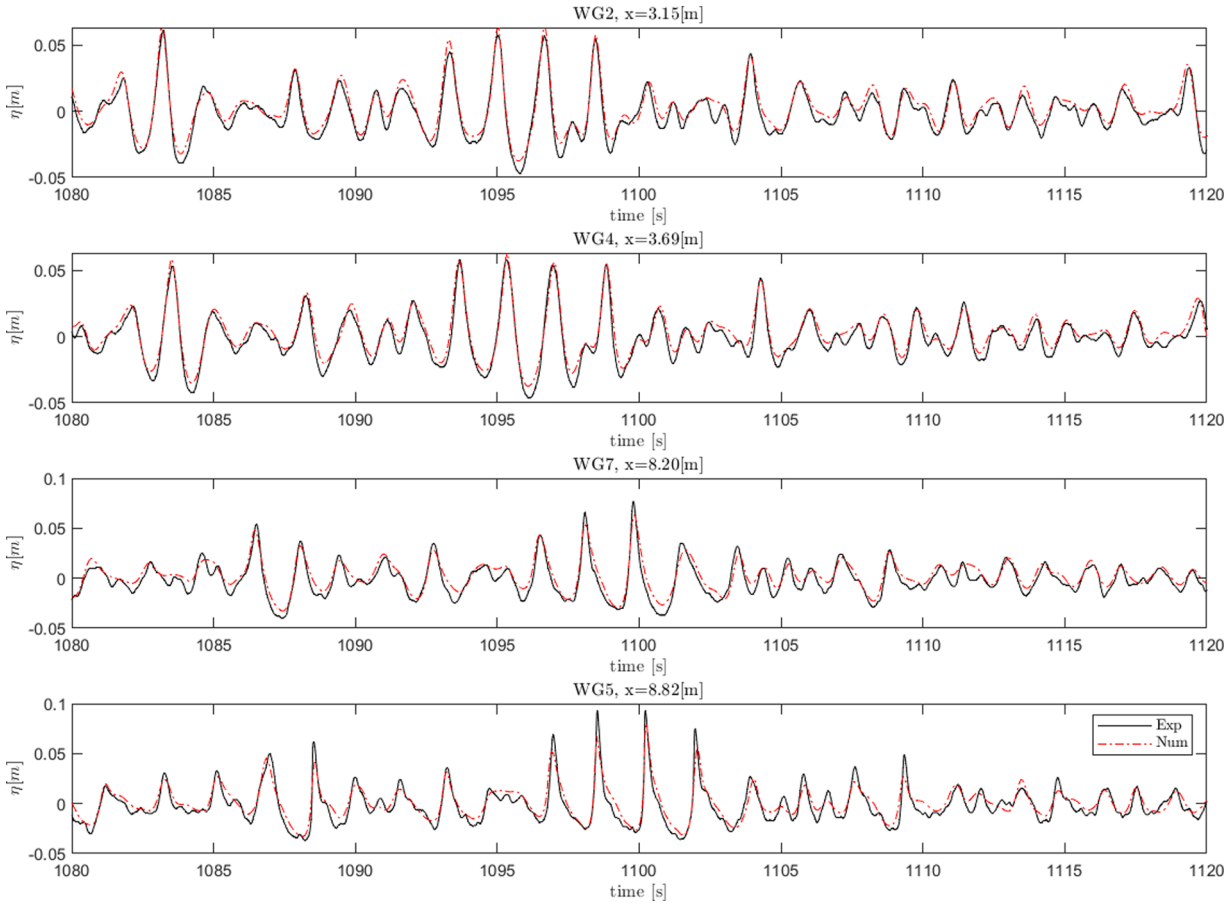

Fig. 6. Zoomed in view between $t = 1080$ss and $t = 1120$s of the comparison of the h time series at WG2, WG4, WG7 and WG5 location for test #17 (results shown in model scale, 1:50).

$$\Pi_{ab} = \{ \frac{-\alpha \mu_{ab} \overline{c_{ab}}}{\overline{\rho_{ab}}} \quad \vec{u}_{ab} \cdot \vec{r}_{ab} < 00 \ \vec{u}_{ab} \cdot \vec{r}_{ab} > 0 \tag{4}$$

where, where $\vec{r}_{ab} = \vec{r}_b - \vec{r}_a$ and $\vec{u}_{ab} = u_b - \vec{u}_a$, $\mu_{ab} = h_{SPH} \vec{u}_{ab} \cdot \vec{r}_{ab} / (\vec{r}_{ab}{}^2 + \varepsilon^2)$, *with* $\varepsilon^2 = 0.01 h_{SPH}$, $\overline{c_{ab}} = 0.5(C_a + C_b)$ is the mean speed of sound, and α is a coefficient (termed artificial viscosity) that determines the rate of viscous dissipation.

Alternatively, the laminar viscosity treatment can be employed in combination with the Sub-Particle Scale (SPS) turbulence model. However, SPS was conceived to be used in 3-D only. It is known that there is unphysical backscatter when using it in 2D, which leads to transfer of energy in the wrong direction from the smaller scales to the larger scales (*Prof. B.D. Rogers, personal communication*).

In weakly compressible SPH method, the pressure, *P*, is obtained through its relation to density by solving the following equation of state (Monaghan, 1994):

$$P = b\left[\left(\frac{\rho}{\rho_0}\right)^{\gamma} - 1\right] \tag{5}$$

where $\gamma = 7$ is the polytropic constant and $b = c_s{}^2 \rho_0 / \gamma$ is defined based on the reference density $\rho_0 = 1000$ kg m-3 and the speed of sound c_s at the reference density. Eq. (5) can be considered as a stiff equation of state, which requires to use very small numerical timesteps to resolve the speed of sound for the weakly-compressible fluid and reduce numerical noise in the pressure filed. In order to increase the computational timestep, the compressibility of the fluid (i.e., speed of sound) is slightly reduced by reducing the speed of sound in Weakly Compressible SPH, while keeping fluctuations in the density field <1%. This is obtained by keeping the speed of sound at least 10 times higher than the maximum velocity in the system. The speed of sound c_s at the reference density is calculated in DualSPHysics as $c_s = coef_{sound} \sqrt{g h_{swl}}$, with $coef_{sound}$ typically ranging between 10 and 20 an being h_{swl}, the depth corresponding to the still water level at the instant $t = 0$ s of the simulation.

The density diffusion term (DDT) presented in Fourtakas et al. (2019) is applied in the continuity equation, to reduce density fluctuations. The key idea is to use the same formulation proposed by Molteni and Colagrossi (2009) but substituting the dynamic density with the total one. In the present simulations DDT is employed using $\delta = 0.1$. The governing mass and momentum equations are numerically solved within DualSPHysics by integrating in time using a numerically stable two-stage explicit Symplectic method with a variable time step that was functionally dependant on a combination of the Courant-Friedrich-Levy (CFL) condition, the forcing terms and the viscous diffusion term.

Boundary limits are implemented in DualSPHysics creating a set of boundary particles that satisfy the same equations as fluid particles, however they do not move according to the forces exerted on them. This approach is called Dynamic Boundary Conditions (Crespo et al., 2007). The version 5.0 of DualSPHysics includes a modification of DBC (the so called mDBC) that is fully described in English et al. (2021). The new approach aims to reduce the large unphysical gap created using DBC due to the overestimated repulsion force. In this case, the boundary interface is first defined away from the layers of boundary particles (defined as $dp/2$ for simple geometries), see black solid line in Fig. 3. It can be noticed in Fig. 3 that, while the initial distance at the edge between fluid (blue points) and boundary particles (grey points) is kept equal to *dp*, the boundary interface is placed $dp/2$ above the boundary particles. A ghost node (red cross in Fig. 3) is projected into the fluid across that boundary

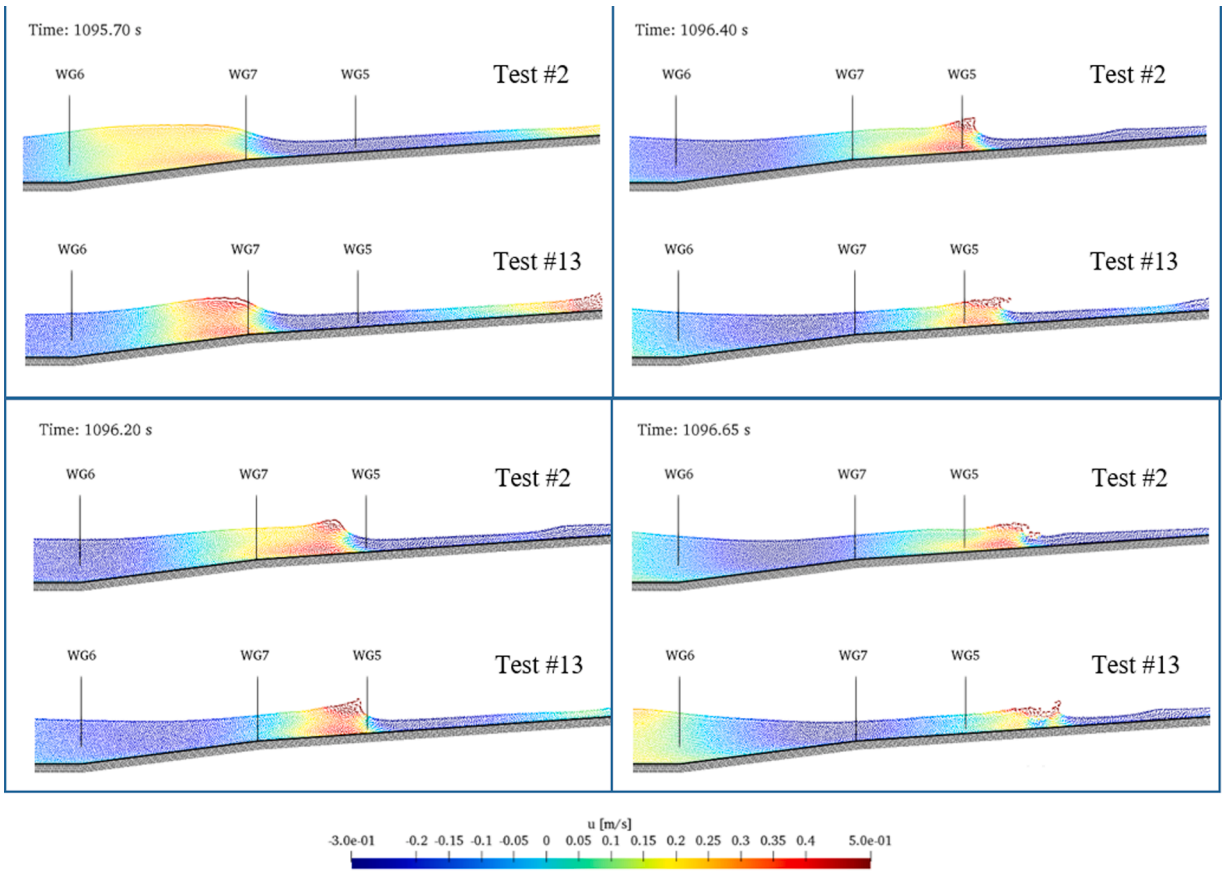

Fig. 7. Snapshots of test cases #2 ($H_{m0,o} = 0.10$ m, $T_p = 1.79$ s, $h_{deep} = 0.30$ m) and #13 ($H_{m0,o} = 0.10$ m, $T_p = 1.50$ s, $h_{deep} = 0.29$ m): detail of the velocity field and wave transformation on the transition and foreshore slope.

interface for each boundary particle. For a flat surface, the ghost node is mirrored across the boundary interface along the direction of the boundary normal pointing into the fluid, meanwhile for boundary particles located in a corner, the normal is defined as the direction between the boundary particle and the corner, hence the ghost node is mirrored through the point of this corner into the fluid region. The density at the ghost node is computed as an SPH approximation from the fluid domain and this value is assigned back to the boundary particle, following an extrapolation method as the one proposed in Tafuni et al. (2018). The same procedure is applied to all the boundary particles interacting with fluid particles in the simulation.

Finally, note, that different techniques to generate and propagate waves are implemented in DualSPHysics, such as: i) the use of boundary particles that move following 1st and 2nd order wave generation with pistons and flaps (Altomare et al., 2017) ii) relaxation zones (Altomare et al., 2018), iii) inlet open boundaries (Verbrugghe et al., 2019) and iv) multi-layered piston wavemaker Altomare et al. (2015b) coupled with external method (called ML-piston). In the present work the first wave-generation scheme is employed: a numerical piston-type wave maker is defined as composed by boundary SPH particle. The wave maker displacement will be imposed by using the same displacement time series as in the physical model tests.

3.2. Numerical model setup

The experimental setup described in §2.1 will be considered to define the numerical domain. Numerical simulations are performed in 2D. The numerical model domain extends from the experimental wave generator ($x = 0$ m), over the foreshore, dike, promenade up to the overtopping tank. The numerical layout for 1:15 foreshore slope is shown in Fig. 3. The geometry of the experimental chute employed for overtopping collection is used (inclination of 1:5 and length equal to 0.25 m) and it can be seen as a left-to-right downward slope behind the promenade. The numerical overtopping tank is longer than the experimental one, to compensate the difference between chute and tank width with the experiment, while keeping the same volume capacity. The shadowed green area in Fig. 4 represents the detecting area employed in the numerical post-processing for overtopping. A dark green layer at the bottom of the tank, just above the mDBC interface, is noticeable: it consists of an initial water volume introduced to avoid numerical instabilities when overtopping SPH fluid particles would drop in an empty tank with high velocities. Overtopping is measured as fluid particles (i.e. volumes) entering the area in time. The FlowTool post-processing code is employed for the scope: FlowTool calculates the number of fluid particles that enters or leaves domains defined by the user. The volume is then easily calculated by multiplying the volume of one particle by the number of particles. Finally, the average discharge is calculated as the total cumulated volume divided by the duration of the test. In this way the differences between experimental and numerical overtopping measurement systems are minimized to allow a fair comparison of the cumulative overtopping volume time series.

All fixed boundaries (red dots) and the wave generator (blue rectangle in Fig. 2 at $x = 0$ m) consists of SPH boundary particles, treated according to the mDBC. The mDBC interface is also depicted in Fig. 4 (black solid line).

Typical model parameters reported in the literature (Altomare et al., 2015a; Lowe et al., 2019; Rota Roselli et al., 2018) have been used in the present simulations, and same values are used in all the simulations (i.e. $coef_{sound} = 20$, $h_{SPH}/dp = 2.1$, $\delta = 0.1$). This means that we did not vary parameters across different test cases to optimize performance. For

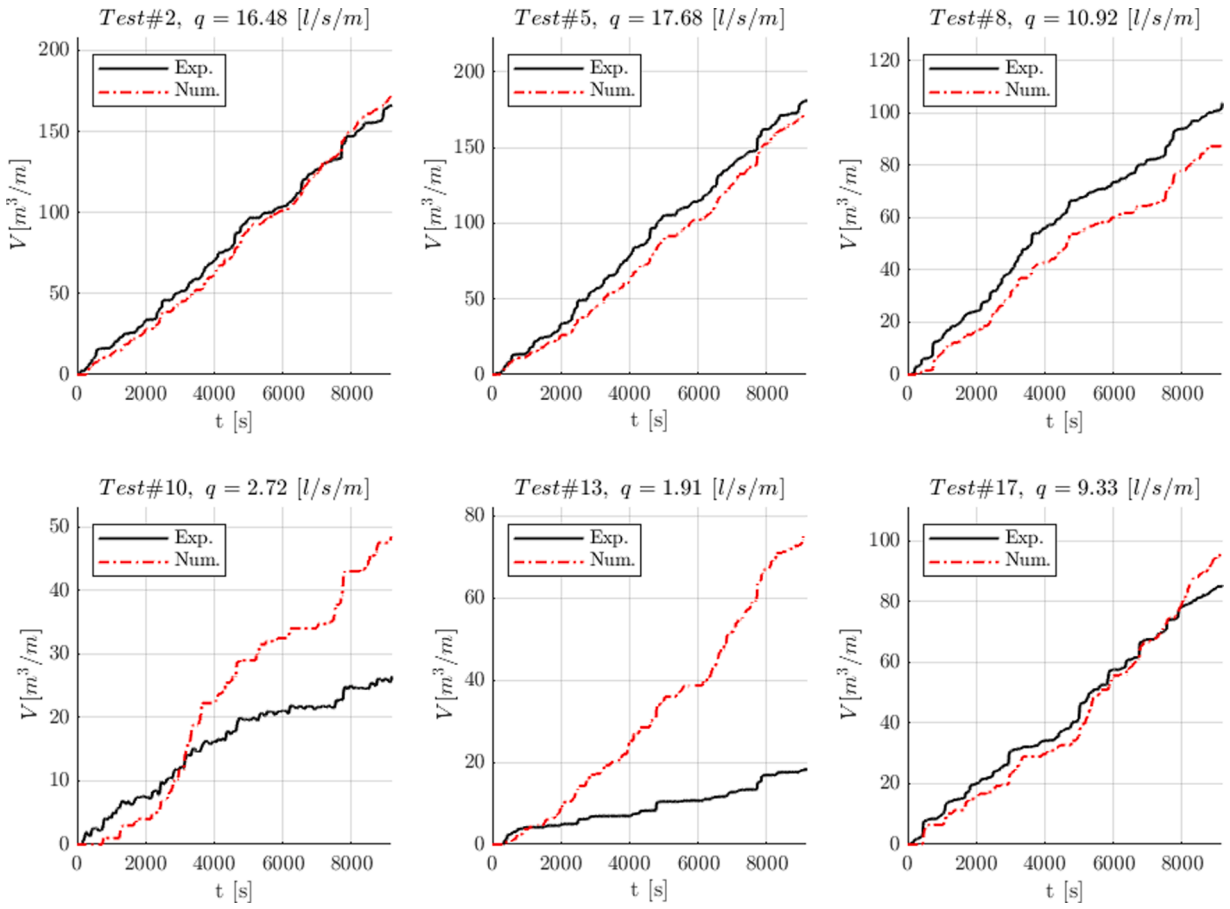

Fig. 8. Cumulative overtopping volumes for test cases #2, #5, #8, #10, #13 and #17. (results in prototype scale, 1:1).

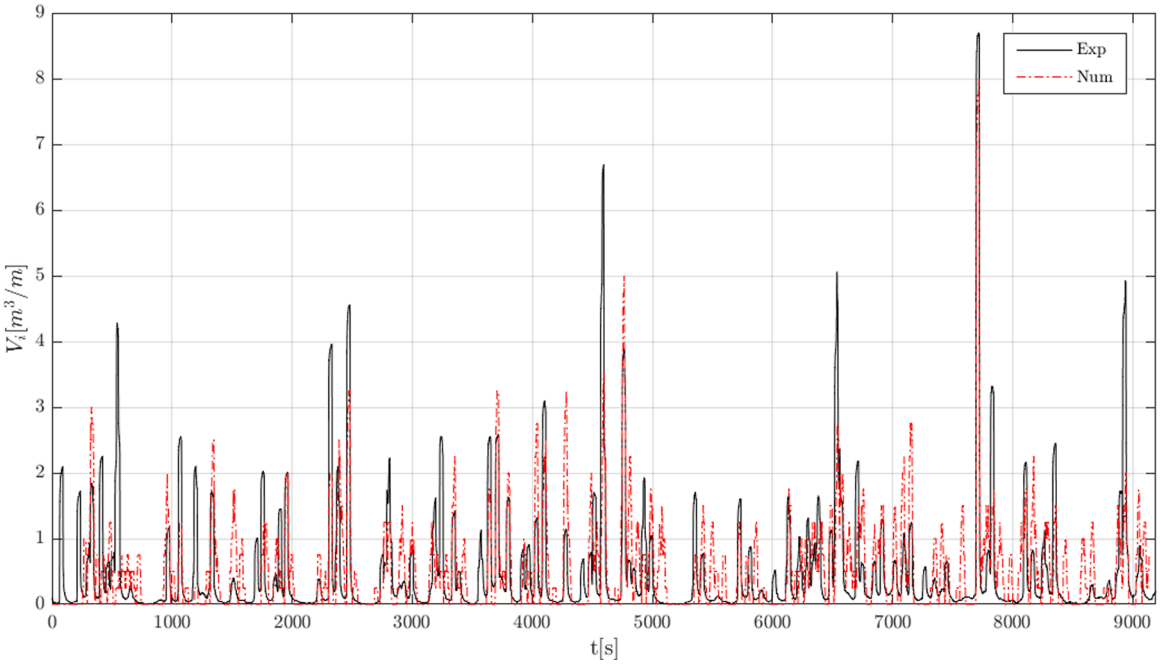

Fig. 9. Time series of individual overtopping volumes for test #2. (results in prototype scale, 1:1).

instance, it is expected that higher resolutions are required to catch the properties of smaller overtopping flows and volumes. However, focus is to provide a rigorous assessment of model performance, while keeping a trade-off between model accuracy and computational run-time for very long-lasting test cases. Several prior studies of wave propagation in SPH demonstrate that the initial inter-particle spacing, *dp*, should be chosen

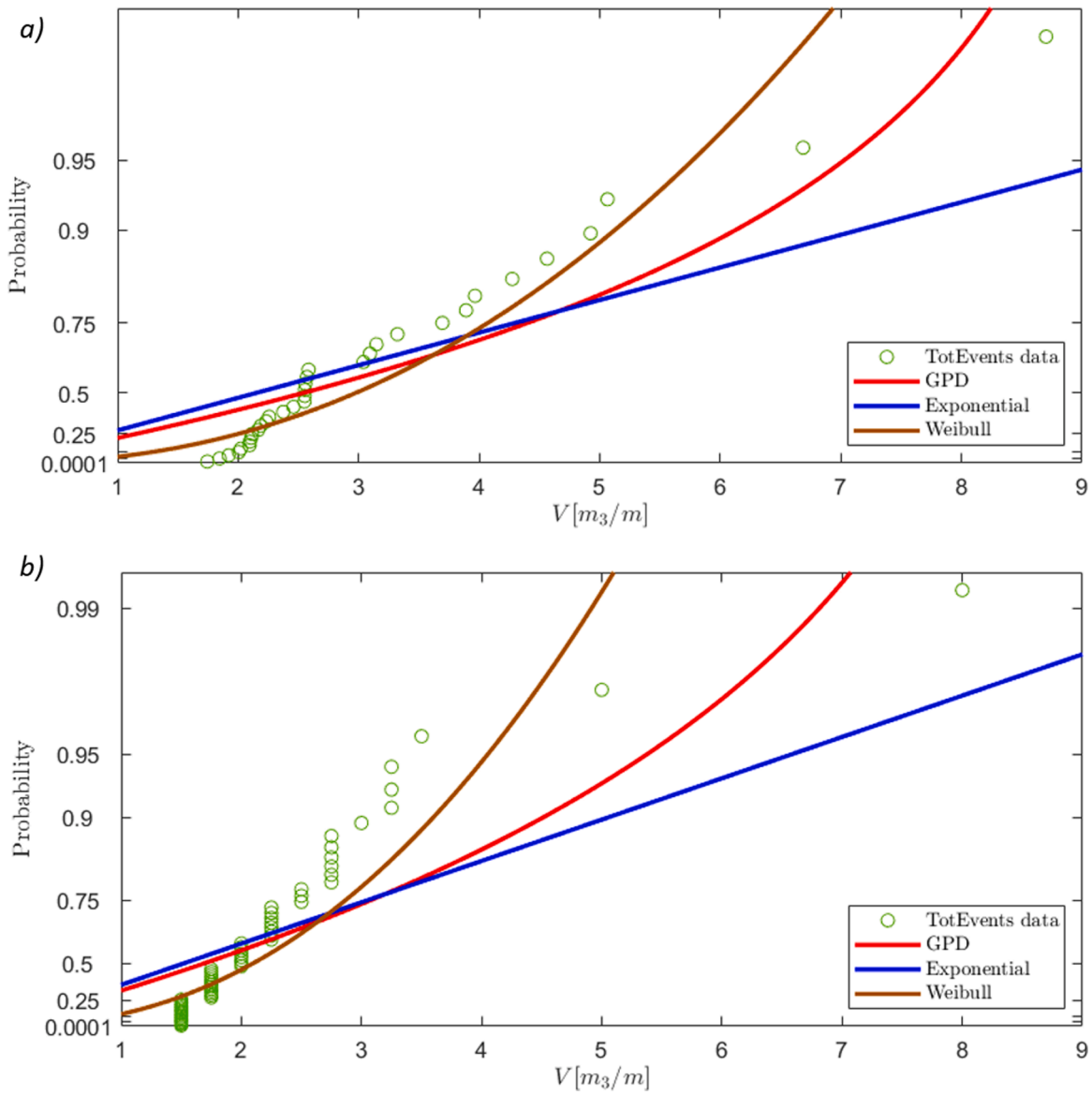

Fig. 10. Probability distribution of experimental (a) and numerical (b) individual overtopping volumes (test #2).

to be about 1/10 of the wave height (Rota Roselli et al., 2018). Considering that the total physical time to be simulated is 1300s, a *dp* equal to 1 cm has been employed, resulting in approximately 32,000 fluid SPH particles: this allows performing simulations in 9.5 h using a NVidia Tesla K40c (2880 CUDA cores, 15 multi-processors) and in 6.7 h when a NVidia GeForce RTX 2080 (2944 CUDA cores, 46 multi-processors) is used. The chosen value of *dp* is based on the generated significant wave heights (order of 0.1 m across all test cases).

Artificial viscosity is used to stabilize the numerical algorithm and increase the long-term accuracy of the numerical simulation (Stansby et al., 2020). The artificial viscosity factor, α, should be chosen to be small enough to allow turbulent motions of size $>dp$ to be properly resolved, but large enough to avoid unstable solutions. It has been proven that artificial viscosity converges to physical viscosity if the number of SPH fluid particles tends to infinite (Monaghan and Kos, 1999; Stansby et al., 2020). The magnitude of the artificial viscosity can be related to the kinematic viscosity of the fluid, as $\upsilon = \alpha c_0 \rho_0 h_{SPH}/K$, being K a coefficient that depends on the dimension of the problem, being equal to 8 for 2D modelling (Monaghan, 2005). As clearly shown in Meringolo et al. (2019), we can relate the Reynolds number, *Re*, characteristic of the specific studied phenomenon in 2D to the artificial viscosity and the numerical resolution as follows: $Re=4(Ma/\alpha)(L/dp)$, being Ma the Mach number and L the reference length of the domain.

A wide range of studies have investigated the optimal value of α in numerical wave flume studies and have consistently found this to be of order 0.01. Therefore, initially the value of 0.01 for α has been employed. However, through a sensitivity analysis we found that model performance was improved for $dp = 0.01$ m while using $\alpha = 0.015$ in DualSPHysics within all runs (see §5.3 for further considerations on α).

3.3. Model performance and validation method

Numerical model validation versus physical model tests is carried out both qualitatively and quantitatively. The qualitative validation comprises the comparison of time series of the water surface elevation, cumulative overtopping volumes, individual overtopping volumes and of the probability distribution of the individual volumes. Yet, quantitative validation is necessary for an objective validation (Gruwez et al., 2020b; Sutherland et al., 2004). Skill score estimators and dimensionless measure of average error are assessed. A first distinction is made here between validation of the incident offshore hydraulic boundary conditions, the error analysis of the total wave time series measured at

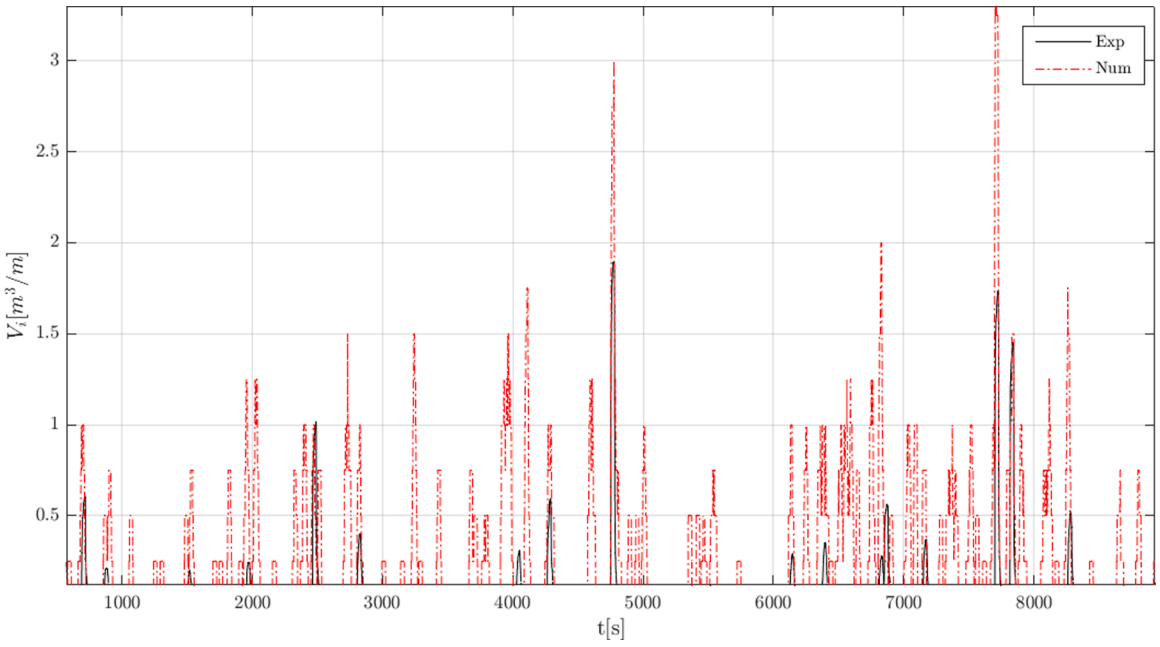

Fig. 11. Time series of individual overtopping volumes for test #13. (results in prototype scale, 1:1).

each wave gauge and the performance in terms of mean overtopping discharge values and overtopping volumes.

For offshore wave characteristics, reflection analysis has been applied to reconstruct the incident wave field using four wave gauges (WG0-WG3 shown in Table 1). The ratio between the so-obtained experimental values of wave height and spectral wave period, $H_{m0,0\text{-}exp}$ and $T_{m\text{-}1,0,o\text{-}exp}$, and the numerical ones $H_{m0,0\text{-}num}$ and $T_{m\text{-}1,0,o\text{-}num}$, is employed to assess model performance at wave generation.

For the total (i.e. incident + reflected) signal at each wave gauge, the method described in Gruwez et al. (2020b) is used. The Willmott's refined index of agreement d_r (Willmott et al., 2012) is defined as follows:

$$d_r = \begin{cases} 1 - \dfrac{MAE}{cMAD}, & MAE \le cMAD \\ \dfrac{cMAD}{MAE} - 1, & MAE > cMAD \end{cases} \tag{5}$$

with scaling factor $c = 2$, MAE is the mean-absolute-error defined by:

$$MAE = \frac{1}{N}\sum_{i=1}^{N}|P_i - O_i|, \tag{6}$$

with N the number of samples in the time series, and P the predicted time series together with the pair-wise-matched observed time series O (for $i = 1, 2, \ldots, n$), and MAD is the mean-absolute deviation:

$$MAD = \frac{1}{N}\sum_{i=1}^{N}|O_i - \overline{O}| \tag{7}$$

where the overbar represents the mean of the time series. The refined index of agreement d_r is bounded by [−1.0, 1.0]. In the present work, d_r is used as a general measure of the model accuracy. A classification of model performance based on ranges of d_r values and corresponding rating terminology is proposed in Table 4 (Gruwez et al., 2020a).

Gruwez et al. (2020b) proposed also to employ pattern statistical parameters to obtain more insight into the origin of the numerical errors (e.g. phase, amplitude). Standard deviation σ is used, which is a measure of the error in amplitude, proportional to the wave energy and hence the wave height. The normalised standard deviation is given by:

$$\sigma^* = \frac{\sigma_p}{\sigma_o} \tag{8}$$

where σ_p and σ_o are the standard deviations of the predicted and observed time series, respectively. To express the difference in wave setup, the normalized bias is used:

$$B^* = \frac{B}{\sigma_o} \tag{9}$$

where B is given by:

$$B = \overline{P} - \overline{O} \tag{10}$$

As last model performance estimator for water surface elevation, we use the correlation coefficient R, defined as follows:

$$R = \frac{\frac{1}{N}\sum_{i=1}^{N}(P_i - \overline{P})(O_i - \overline{O})}{\sigma_p \sigma_o} \tag{11}$$

which is a measure of the phase similarity between the time series. The time series of the wavemaker displacement employed both in the experimental and in the numerical modelling have been used to synchronize the two signals and avoided induced phase errors. Each numerical run had a duration of 1300 s (physical time), whereas the duration of experimental time series varied as function of the mean wave period (1000 times longer). For the sake of comparison, the only the first 1300 s of each experimental time series have been considered. Since the experimental and numerical time series have different sampling frequencies, 80 Hz and 20 Hz respectively, the experimental time series have been down sampled to 20 Hz.

For the assessment of model performance in terms of mean discharges and volumes, ratios between predicted (i.e. numerical) and experimental values have been calculated. Besides, the geometric mean and standard deviation are employed (Altomare et al., 2016; Goda, 2009; Yuhi et al., 2021) for assessment of the mean discharge prediction.

The geometric mean μ_q is defined as follows:

$$\mu_q = exp\left[\frac{1}{M}\sum_{i=1}^{M} lnx_i\right]; \text{ with } x_i = \frac{q_{num,i}}{q_{meas,i}} \tag{12}$$

where M is the number of tests, $q_{num,i}$ and $q_{meas,i}$ are respectively the i th

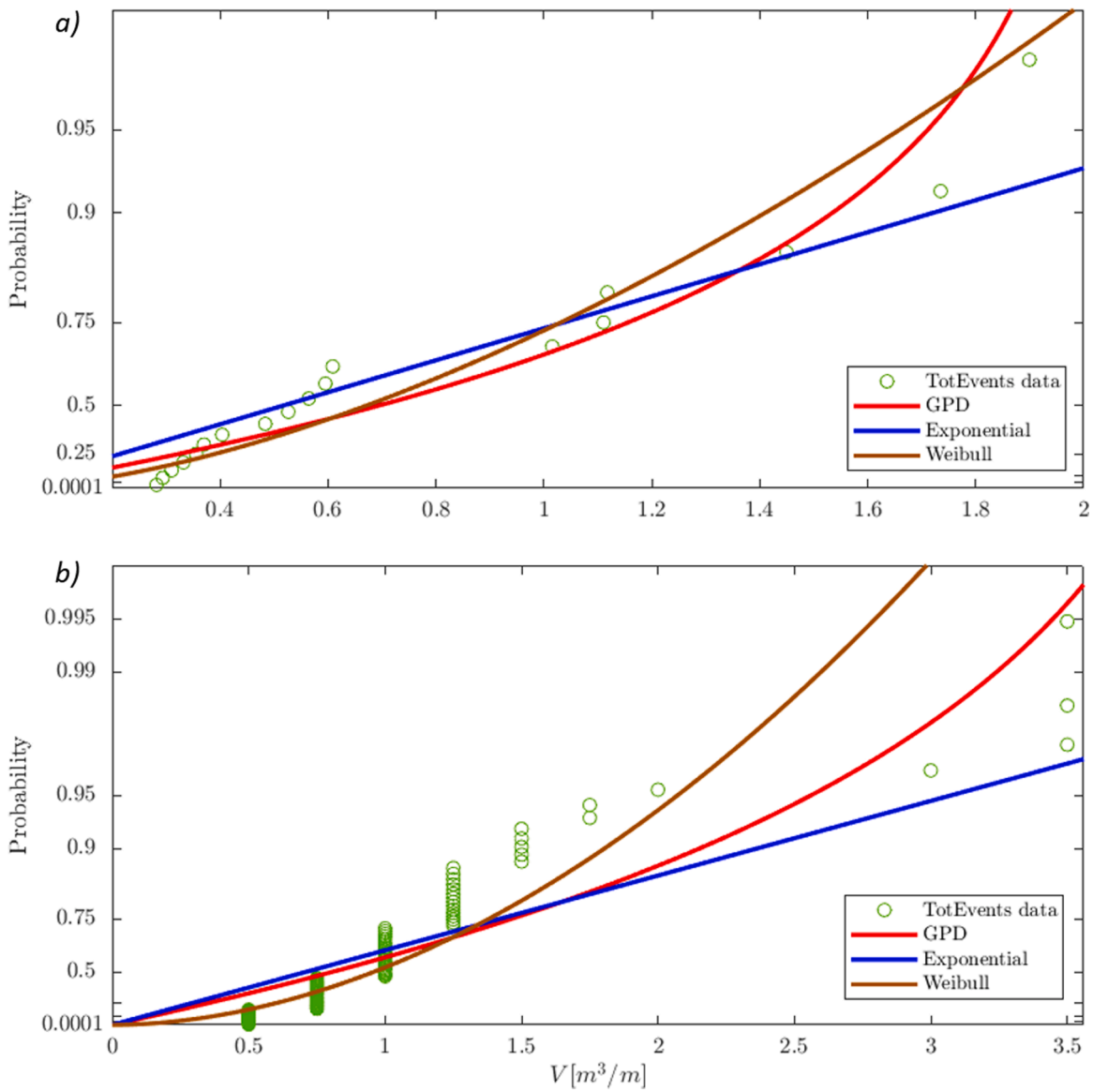

Fig. 12. Probability distribution of experimental (a) and numerical (b) individual overtopping volumes (test #13).

predicted and measured mean overtopping discharge. The scatter of the data is assessed through the geometric standard deviation σ_q that is calculated as the exponential value of the standard deviation of the logarithm:

$$\sigma_q = exp\left\{\left[\frac{1}{M}\sum_{i=1}^{M}\left((lnx_i)^2 - \left(ln\mu_q\right)^2\right)\right]^{0.5}\right\} \tag{13}$$

Considering a quantity normally distributed, 90% of the data will be contained in the range between the mean divided by 1.64 times σ_q and the mean multiplied by 1.64 times σ_q.

4. Results

4.1. Qualitative comparison

The numerical results have been compared qualitatively in time domain to the experimental ones. Time series of water surface elevation at different sensor locations and cumulative overtopping volumes are shown.

Numerical and experimental time series of water surface elevation, measured at the location corresponding to the experimental wave gauges WG2, WG4, WG7 and WG5 are depicted in Fig. 5 for a time window of 200 s.

The numerical time series of the surface elevation are computed according to the interpolated mass along a vertical grid of measurement points (that forms a sort of numerical wave gauge). The Z-position of the nodal points where there is a change between fluid and void (checking that the nodal mass is higher than a given reference mass) is considered as the surface elevation.

A zoomed in view, between $t = 1080$s and $t = 1120$s is shown in Fig. 6, which encompasses the higher peak depicted in Fig. 5. The time series match graphically very well, especially for those wave gauges located offshore (WG2, WG4). In general, the wave crests are well modelled, while the numerical wave troughs look less deep than the experimental ones, however the differences are similar to or smaller than the same model resolution. Overall, wave transformation, including shoaling and breaking seems to be reproduced accurately. Here, results from test #17 only are shown. All other tests show similar level of agreement with experimental data. The results shown in Figs. 5 and 6 are expressed in model scale.

Snapshots of the numerical test cases #2 and #13 are reported in Fig. 7: the area comprising the transition slope and foreshore slope is

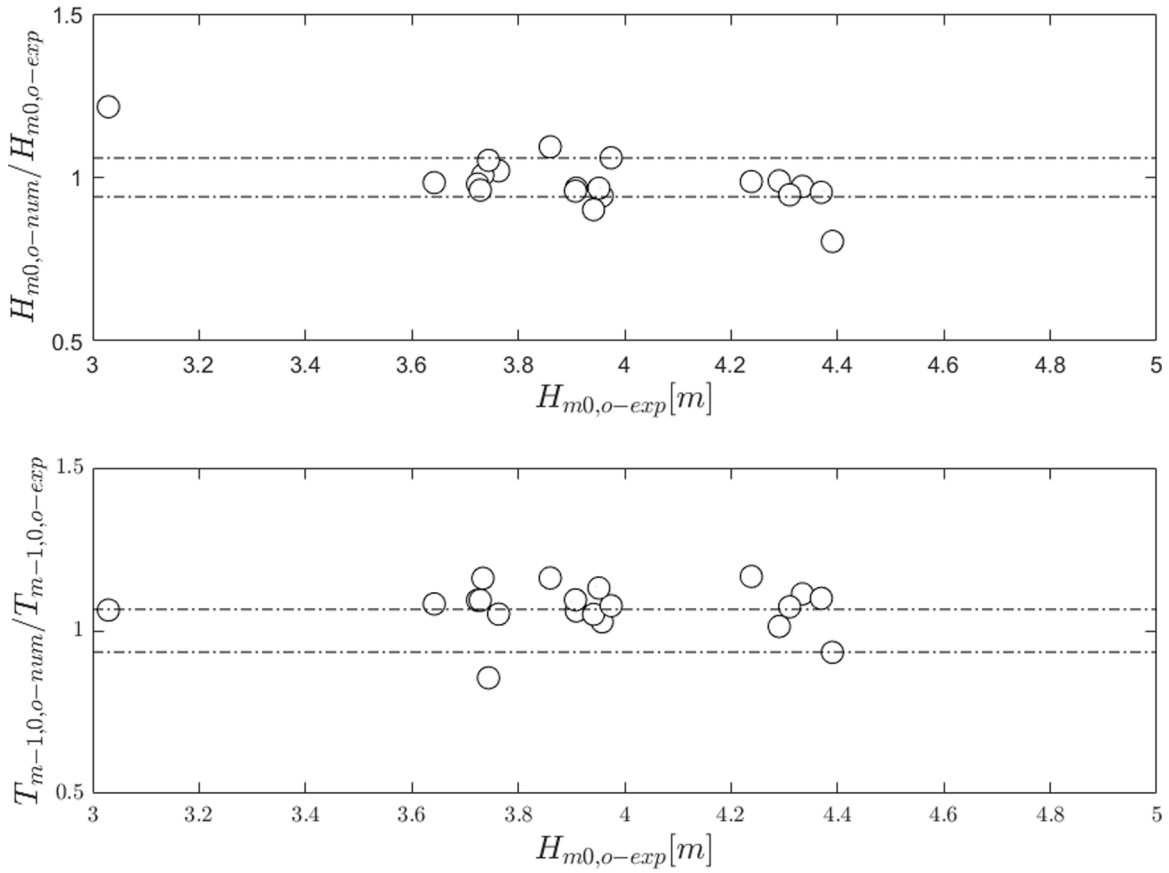

Fig. 13. Error of incident offshore significant wave height and period. The dash-dotted lines are calculated based on the coefficients of variations from EurOtop (2018).

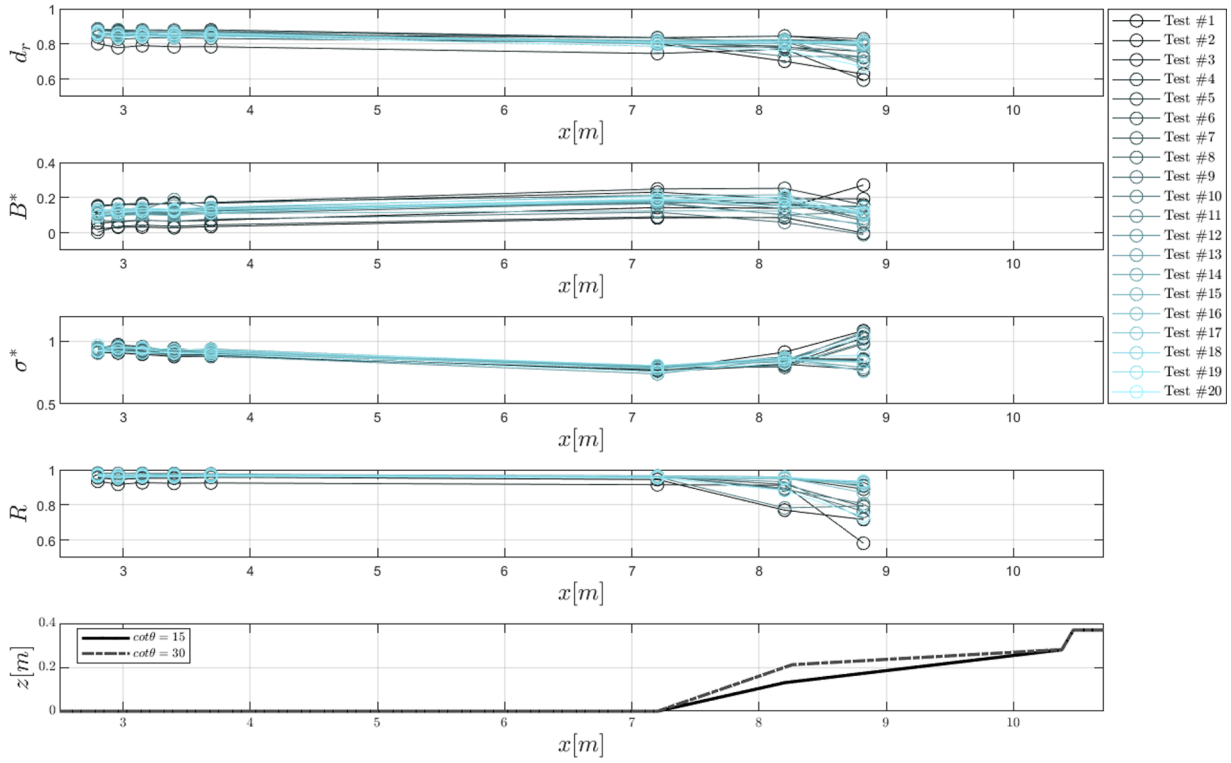

Fig. 14. Model performance estimators for water surface elevation evaluated for each test case. From top to bottom: d_r, B*, σ* and R. Last image provides a scheme of the foreshore and dike layout.

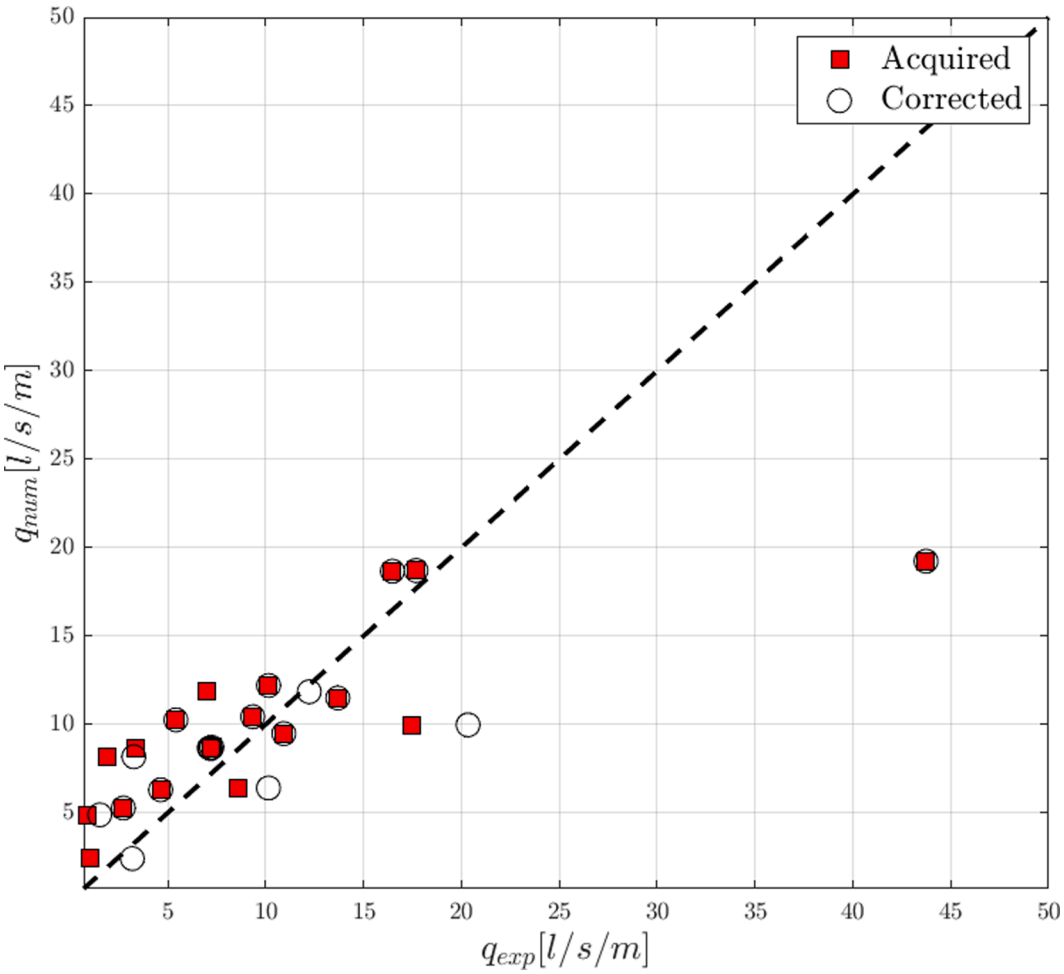

Fig. 15. Comparison of experimental and numerical mean overtopping discharge values. The comparison is made with acquired overtopping discharges untreated (red squares) and the ones corrected to compensate scale effects (white circles). (For interpretation of the references to colour in this figure legend, the reader is referred to the web version of this article.)

represented, including locations of WG6 (start of the transition slope), WG7 (start of the foreshore slope) and WG5 (breaking zone); the field of the horizontal velocity is depicted. The two cases have the same offshore wave height (0.1 m in model scale) but they differ 0.01 m (0.50 m in prototype scale) in water depth and have different wave periods (1.79 s for test case #2 and 1.5 s for test case 13, respectively). In both cases, it can be noticed that already at WG7 the horizontal velocity profile is quite uniform, indicating that we are already in shallow waters and the orbits of the fluid particles are flattened. At WG5 the waves start to break to form the bore that will run over the rest of the foreshore and reach to dike to overtop it.

Cumulative and individual overtopping volumes are reported in prototype scale hereafter, to allow the classification with respect to tolerable overtopping design criteria as proposed in literature (EurOtop, 2018). The acquired raw experimental signal showed some noise, mostly due to surface oscillations inside the tank provoked by the overtopping volumes dropping from the chute extreme. To remove this noise that might affect the further peak detection, a third-order median filtering was applied to the raw signal. The numerical and experimental time series of cumulative overtopping volumes are depicted in Fig. 8 for six selected test cases (#2, #5, #8, #10, #13 and #17) according different mean discharge values ranging from 1.91 l/s/m (test #13) to 17.68 l/s/m (test #5). Results are expressed in prototype scale. A general agreement is noticed between numerical and experimental results, with an overestimation of overtopping volumes in those cases characterised by lower discharges. The discrepancy between DualSPHysics and experiment increases when the overtopping decreases, fact that was expected since the same model resolution has been employed regardless the differences in measured overtopping flows amongst the all cases. Notice that the volume measured numerically is defined by a nodal point and given by dp*dp in 2D, so that, this is our minimum unit (numerical error) when measuring volume with DualSPHysics.

Time series of individual overtopping volumes are compared in Fig. 9, for test #2. Results are expressed in prototype scale. For numerical modelling the individual volumes are directly measured using the post-processing tools available in DualSPHysics, as volumes entering the overtopping measuring area (green shadowed area in Fig. 4). For experimental modelling, the individual volume time series is derived from the cumulative time series: a time window of 4 s (roughly one wave period at the dike toe, in model scale) is employed to separate different events.

To identify each individual volume a peak detection subroutine has been employed in Matlab. Although the time series do not completely match, certain similarities can be appreciated. For instance, the time of the largest peaks of the series are very well reproduced numerically as their amplitude. It must be remarked here that overtopping modelling and detection in DualSPHysics is strictly related to the numerical model resolution. Moving from continuum to a discrete representation of the fluid, determines the minimum individual overtopping volume that can be simulated. For a resolution of 1 cm, this volume corresponds to 250 l/s in prototype. All measured numerical volumes will be therefore multiple of this quantity. Based on this, all peaks are identified above a

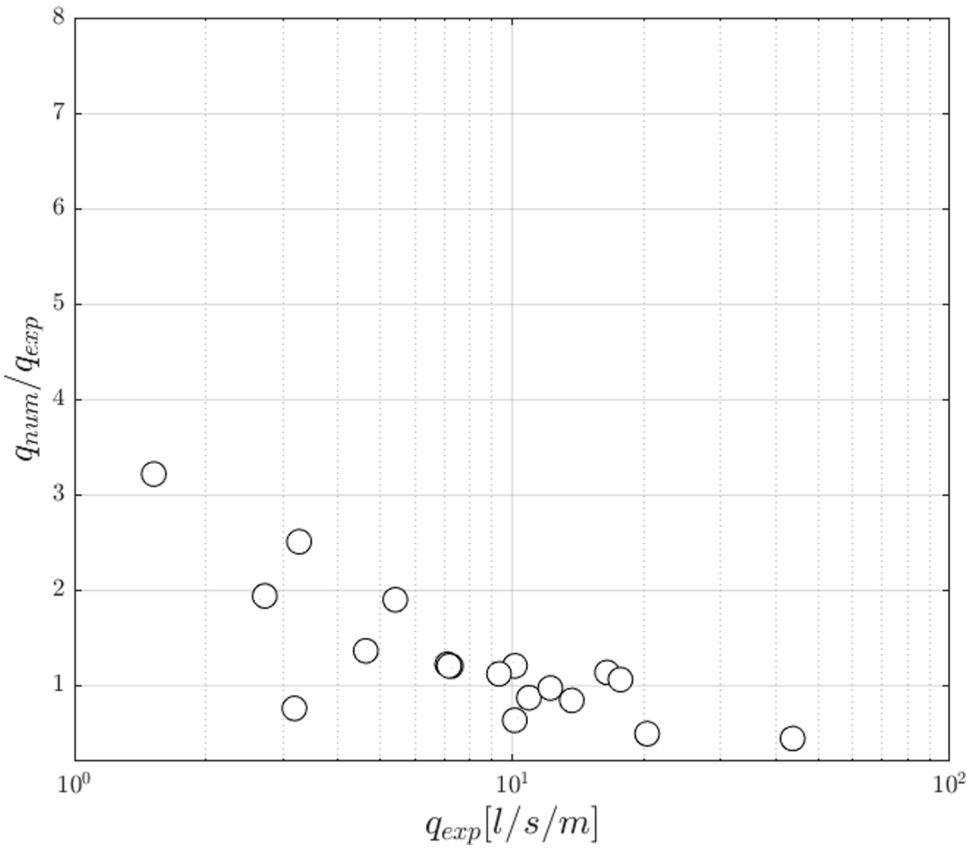

Fig. 16. Error in mean overtopping discharge. Experimental results refer to the those corrected for compensating scale effects.

threshold of 250 l/m (in prototype scale). Similar comparison, for test #13, is plotted in Fig. 11. Here, a large deviation of the numerical results from the experimental ones is noticed, confirming the low performance of the model, with the setup described in § 3, for case #13, which exhibits the lowest measured overtopping discharge and lowest individual volumes.

Finally the probability distribution of individual overtopping volumes is plotted in Fig. 10, for experimental (a) and numerical volumes (b) respectively, for case #2. The distributions are compared with three probability distribution functions: exponential, Generalized Pareto distribution (GPD) and the two parameter Weibull distribution. The data sample is using the significant volume, the upper 1/3 tail of the distribution of the volume (e.g., Vi $>$ $V_{1/3}$) of each test. Both experimental and numerical data are fitted by a Weibull distribution, which is the one usually employed for individual overtopping volumes (EurOtop, 2018). Same analysis, but for case #13, is depicted in Fig. 12. Experimental results show a very low number of identified volumes (peaks), as also noticeable in Fig. 11, fact that lead to low accuracy when fitting with any standard distribution. More peaks are identified in the numerical model, however it can be seen that they are clustered in groups, multiple of the initial model resolution (see discussion above).

4.2. Model performance

The model accuracy is assessed based on estimators and pattern statics described in §3.2, to provide a measure of the numerical model performance.

The performance of the model to match the incident offshore wave field is expressed as ratio of the numerical values of spectral wave height and period to the experimental ones. Results are plotted in Fig. 13 along with confidence intervals. These values have been calculated using the coefficients of variation for wave height and period proposed in EurOtop (2018), namely σ'(H_{m0})=±0.036 and σ'($T_{m-1,0}$)=±0.04. They are multiplied by 1.64, so to obtain a 90% confidence interval (assuming a Gaussian distribution of the error). Except for very few cases, overall the wave height is well predicted by the numerical model. Larger deviation is shown for the smaller wave height, probably due to the selected model resolution not able to catch the smallest waves in the wave train. Wave period values show larger deviations, however within reasonable ranges.

The model accuracy in simulating the water-surface elevation at each experimental wave gauge location has been assessed in terms of 4 parameters described in §3.2: the refined index of agreement d_r, the normalized bias B^*, the normalised standard deviation σ^* and the correlation coefficient R. The evolution of these parameters along the flume is depicted in Fig. 14.

The evolution of d_r along the flume is very similar for all cases 20 test cases: it remains constant before the foreshore and along it until the breaking zone (WG0-WG7, $x<\approx 8$ m), but decreases slightly at WG5, already after breaking. This is in agreement with the qualitative analysis performed in §3.1.1. The index of agreement ranges between 0.79 and 0.89 for all offshore wave gauges, namely WG0-WG4, showing hence a *very good* performance. At WG6, located at the beginning of the transition slope, values of d_r lower than 0.8 are measured only for test cases #3, #4 and #20. The performance at WG7 is good or very good, ranging d_r between 0.70 and 0.84, being the lowest value calculated for test #1. The same test is amongst those ones with the lowest performance at WG5 (rating d_r 0.63), together with test #3 (rating d_r 0.59) and test #20 (rating d_r 0.67). In any case the model performance at WG5 can be rated as *reasonable*, based on the classification reported in (Gruwez et al., 2020a), see Table 4 .

The pattern statistics B^* and s^* quantify the numerical model accuracy in terms of wave setup and wave height. Overall, the values of B^* are constant along the flume, with larger deviations at WG5, ranging

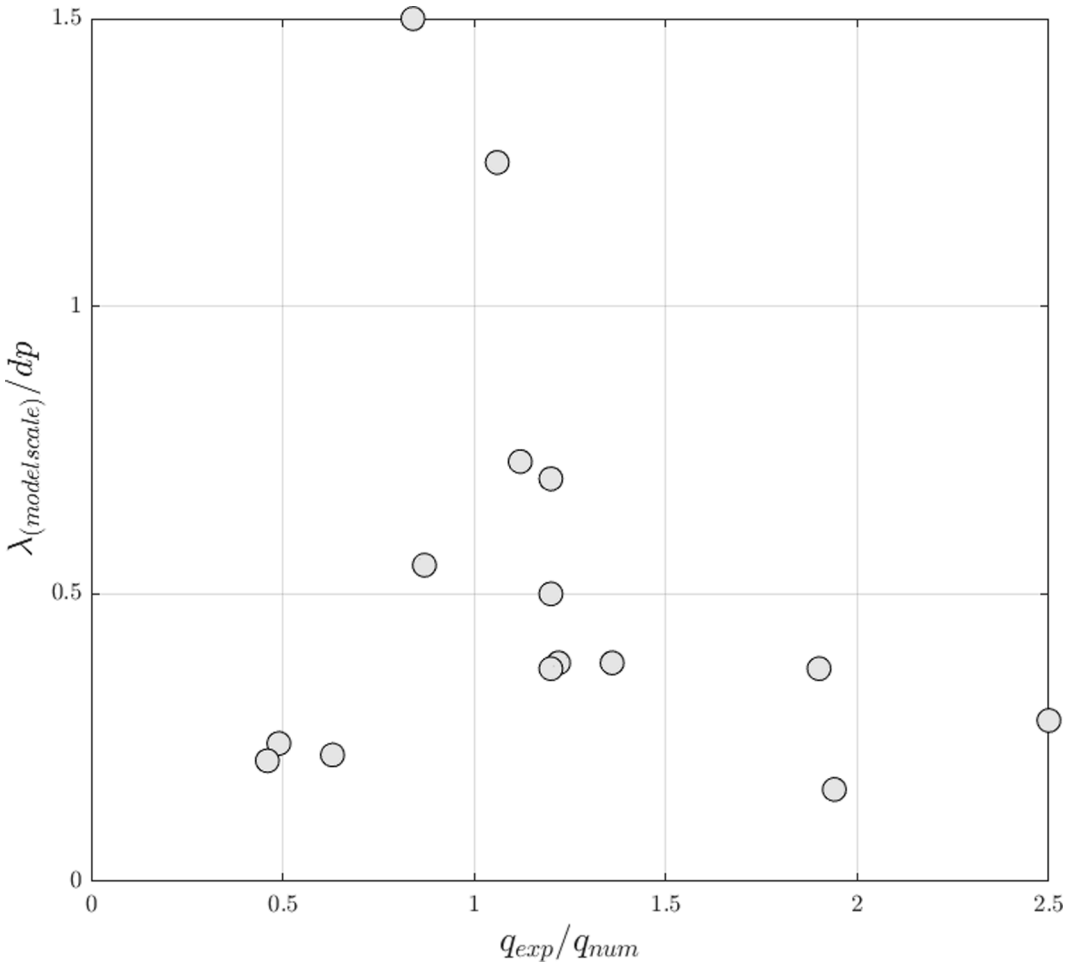

Fig. 17. Ratio between experimental and numerical overtopping discharge vs the ratio between the overtopping flow depth (when available) and the model resolution.

between −0.01 and 0.27. The error in amplitude express by $s*$ (or better 1-$s*$) is low, ranging between 0.76 (at WG5) and 1.08 and confirming that, even with the selected model resolution, the numerical wave height and hence the associate wave energy are in close agreement with the experiments. Finally, the correlation coefficient R is employed to look more in detail to the model accuracy in terms of phase. The phase accuracy shows a different trend than other error estimators. It is quite constant along the flume except at WG7 and WG5, where results are more disperse (averaging all cases, $R \approx 0.96$ at WG0-WG6, 0.92 at WG7 and 0.84 at WG5). The phase prediction decreases in the shoaling and breaking area, but not uniformly for all cases. Most probably the lower agreement is due to the energy transfer from shorter to longer wave components in SPH, which does not match the experimental results. This is also reflected in the errors calculated in the previous section on the incident wave period. Actually it seems that long wave components are present in SPH simulation, where they are absent or minor in the experiments.

The predicted mean discharge values are compared with the measured ones in Fig. 15, where results from both experimental raw acquired data and data corrected for scale effects compensations are depicted. For low discharges actually the experimental corrected values seem to agree better with model prediction. Calculated geometric μ_q mean is equal to 1.07 with a geometric standard σ_q deviation of 1.31. Assuming a normal distribution this means that the uncertainty of the numerical prediction can be estimated by a 90% confidence interval defined within a range between 0.5 and 2.3 times the ratio numerical to experimental discharges. The latter one calculated for each test case is plotted in Fig. 16. It can be noticed as the discrepancy between numerical and experimental results depends on the mean discharge values to simulate. In particular, the numerical model tends to overestimation and this increases as the discharge decreases. For discharges lower than 4 l/s/m, the predicted overtopping is more than twice the measured one. This result was expectable considering the initially employed numerical resolution and is confirmed in Fig. 17 where the ratio between experimental and numerical overtopping discharge is plotted against the ratio between the overtopping flow depth (when available and expressed in model scale) and the model resolution. For values of $\lambda_{(model\ scale)}/dp \geq 0.5$, the ratio q_{exp}/q_{num} ranges between 0.9 and 1.2, while either larger underestimation or overestimation is noticed for $\lambda_{(model\ scale)}/dp < 0.5$.

The comparison of experimental and numerical individual overtopping volumes is presented in Fig. 18. For each test case the maximum individual volume V_{max}, $V_{1/10}$ and $V_{1/3}$ are shown, corresponding to the maximum individual volume, the upper 1/10 of the volume distribution and the upper 1/3 of the volume distribution, respectively. Larger scatter is shown for V_{max}, while smaller scatter is shown $V_{1/3}$. The maximum volume is actually a quite random or stochastic value, very dependent on the time series and in most cases not repeatable experimentally. For this uncertainty, to model the largest volumes is challenging even in a very sophisticated and well validated numerical model. Errors between numerical predictions and experimental values are depicted in Fig. 19 . Once again, larger errors are shown for lower overtopping values. However, the differences are quite limited (DualSPHysics provides volumes twice as the experimental one, in the worst case). Similar trend is also noticed when the number of overtopping

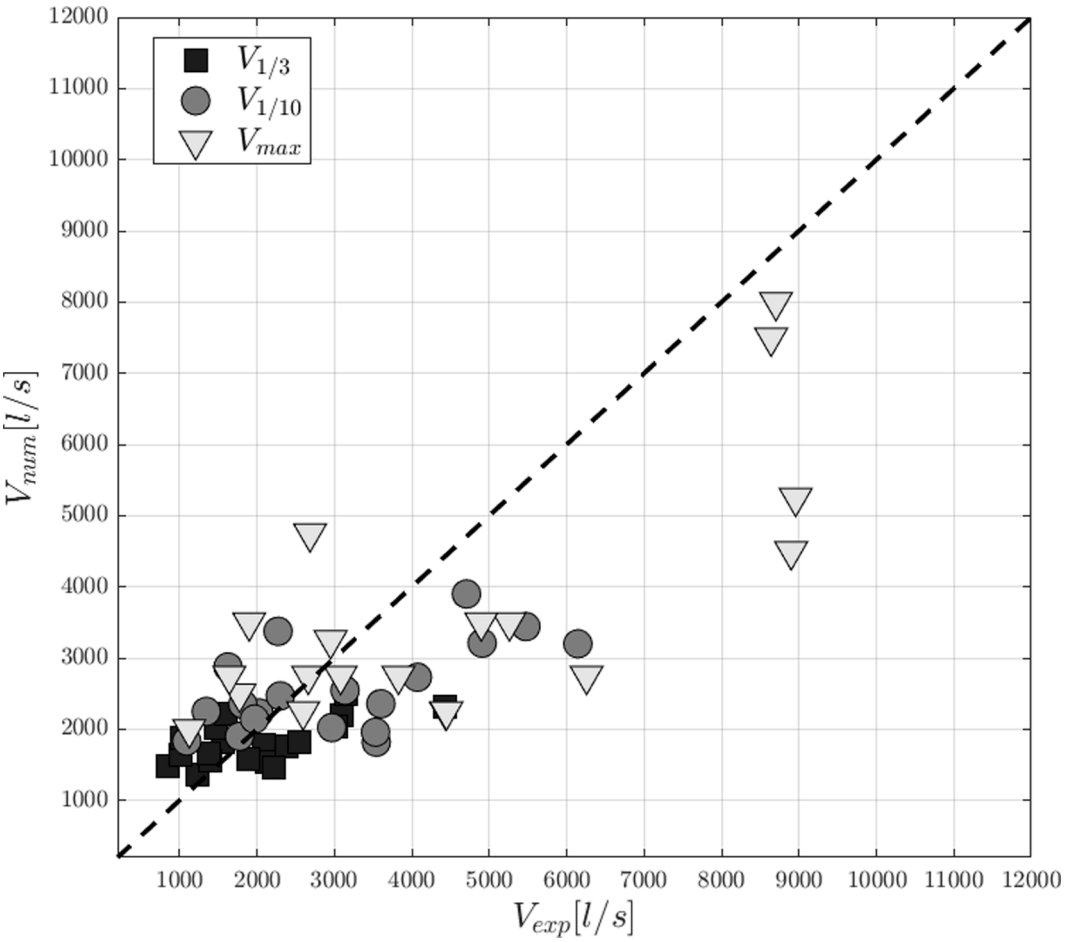

Fig. 18. Comparison of experimental and numerical overtopping volumes. For each test case the maximum individual volume Vmax, V1/10 and V1/3 are shown.

waves, *Nov*, is calculated for both numerical and experimental modelling, with the only difference that DualSPHysics tends in general to overestimate the number of overtopping waves (see Fig. 20).

5. Discussions (model resolution, possible improvements, coupling)

5.1. Adaptivity and model resolution

Adaptivity or variable resolution can be defined as the capability of a numerical scheme to use elements (meshes, computational nodes) of variable size to discretise the studied domain. To simulate large domains and multi-scale problems, adaptivity is crucial. Nevertheless, while mesh-based approaches present robust implementations of variable resolution, in SPH most of the existing solvers, including DualSPHysics, are still based on uniform resolution, despite some attempts already made (e.g. Spreng et al., 2020). It is unclear in SPH what is the best approach to resolve adaptivity, defined still as one of the main Grand Challenges by SPHERIC community (Vacondio et al., 2021). In simulating wave overtopping, Shao et al. (2006) noticed already that the performance of SPH-based in comparison with Eulerian models is affected by the lack of variable resolution in SPH. The author stated that "*further improvement of the spatial resolution in the SPH model will be expected to provide better predictions of the wave overtopping rate*". Recently, Gruwez et al. (2020b) drew similar conclusion when comparison performance of DualSPHysics with OpenFoam and SWASH models. Using only a fixed resolution, SPH has limits when it is applied to the simulation of wave-structure interaction problems where the horizontal scale is much larger than the vertical scale. Wave overtopping is one of this cases: large domain is needed for a correct wave propagation and transformation, however overtopping flows are usually characterized by very thin and often turbulent water layers passing over the structural crest. To cope with it, either very fine resolution is used, which is possible thank to GPU technology, or coupling between SPH solvers and wave propagation or spectral solvers have been implemented (Altomare et al., 2018; Altomare et al., 2018b; Oger et al., 2014; Verbrugghe et al., 2018).

In the present work a uniform and fixed model resolution of 1 cm has been used for all test cases, regardless the overtopping flow characteristics, which are not resolved. To model accurately each individual overtopping flow over the dike crest would require a resolution 5 or even 10 times finer, which will result in a very expensive modelling for a model run of 1000 waves (≈1300s). Other works have already demonstrated SPH to lead to accurate modelling of the hydrodynamics of run-up or overtopping flows (Lowe et al., 2019). Focus of the present work is instead to prove that SPH can be used as a preliminary design tool and hence can provide a fast but acceptable and reasonable information of mean overtopping discharges and overtopping volumes. Still, for sake of completeness, a test case has been selected to analyse the model response to variation of numerical model resolution. Results are reported in Appendix A. The selected test case is one of the cases with largest deviation between experimental and numerical model results, namely case #13. The following conclusions can be drawn after the sensitivity analysis: the performance of the model is deeply affected by the value of the artificial viscosity factor, α; it is not sufficient to increase the resolution to reduce the numerical error without modifying the value of α.

Finally, it has been shown in the previous sections that, for fixed

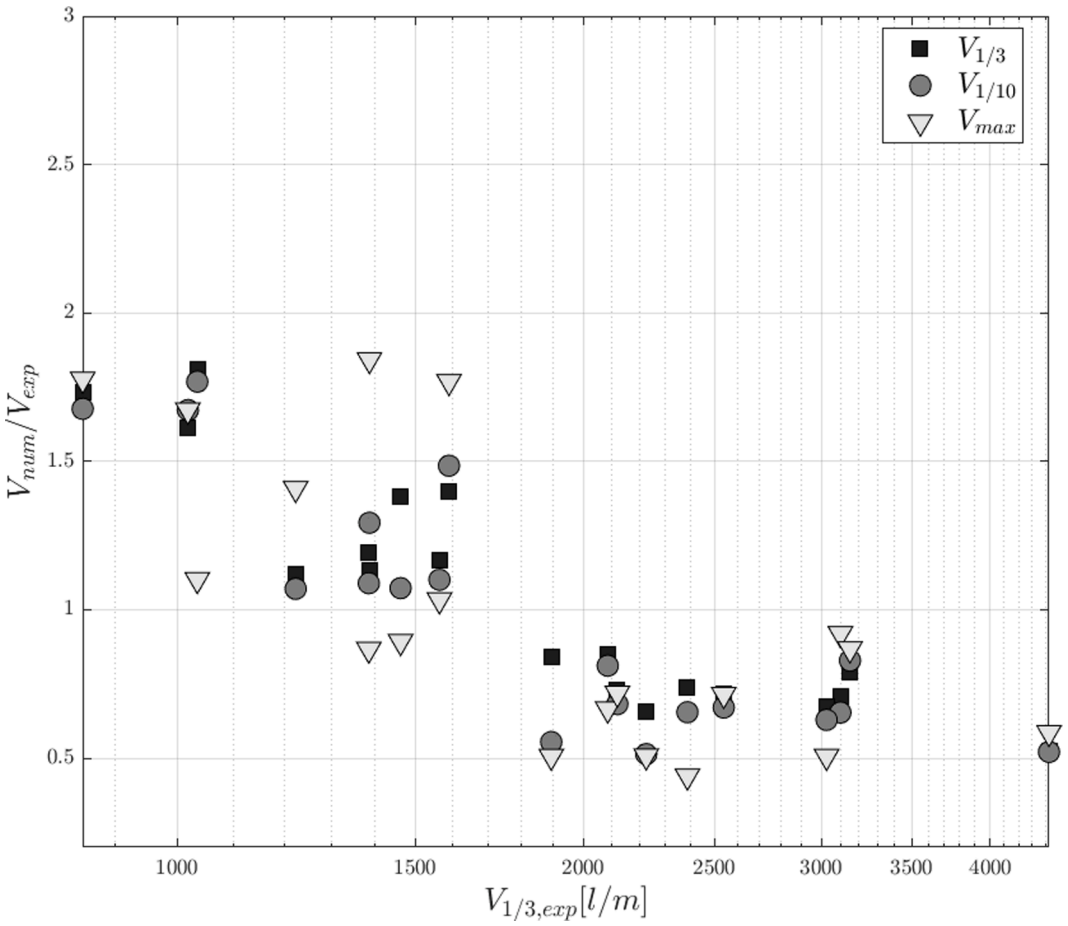

Fig. 19. Error in individual overtopping volumes. For each test case the maximum individual volume V_{max}, $V_{1/10}$ and $V_{1/3}$ are shown.

model resolution, the deviation of the numerical model prediction with respect to the experimental results increases when the overtopping discharge and volumes decrease. Nonetheless, the numerical error for $dp = 0.01$ m is comparable to uncertainties of overtopping prediction when semi-empirical formulation are applied, where typically this uncertainty increases when discharges decrease (EurOtop, 2018).

5.2. Boundary conditions

Dynamic Boundary Conditions (DBC) present some drawbacks such as an over dissipation that leads to un-physical large boundary layers. However, using mDBC as in this work, a more accurate and smooth pressure field is achieved and the unphysically large boundary layer is avoided, as demonstrated in (English et al., 2021). This aspect might be crucial in certain simulations, e.g. wave overtopping. It is well known that overtopping depends exponentially on the structural freeboard, defined as the vertical distance between the dike crest and the still water level. If DBC is applied, to compensate the created large boundary layers, the dike crest or any significant geometrical feature have to be lowered ad-hoc, usually by a quantity that is proportional to the smoothing length (Altomare et al., 2014). Besides, the typical pressure noise associated to DBC would affect the hydrodynamics of the simulated overtopping flows. We selected test case #2 to compare mDBC with DBC results. The time series of cumulative overtopping volume for test case #2 are depicted in Fig. 21. The geometrical freeboard in the DBC has been kept the same as in mDBC, to show the effects of the unphysical boundary layer created by DBC on thin layer of fluid particles. The reader can appreciate that applying DBC with no further adjustment, the volumes are far smaller and the final total volume and consequently the mean discharge resulted one order of magnitude smaller. Two snapshots of the numerical model simulation for DBC and mDBC are shown in Fig. 22 for two time instants. The fluid density field is shown (related to pressure for the equation of state) for the two cases. In the DBC case the noise in the density field close to the solid bottom can be appreciated and the detachment of the tip of the bore (thin layer of fluid) from the bottom is noticeable. This actually corresponds to the unphysically large boundary layer to which we refer above. For $t = 1095.50$ s, the reader can appreciate how in the mDBC case the water is overtopping the dike, while no overtopping is produced in the DBC case.

The use of mDBC has therefore three main advantages: 1) the geometrical layout is not represented uniquely all over the domain by the boundary interface; 2) the fluid velocity, density and pressure are more accurately resolved close to the boundaries; 3) unwanted unphysical detachment between fluid and boundary is prevented.

5.3. Artificial viscosity

Previous studies on wave propagation and wave structure interaction showed that a value of the artificial viscosity factor α=0.01 led to accurate simulations (Altomare et al., 2017, Altomare et al., 2015a; Crespo et al., 2017; Rota Roselli et al., 2018). However, while wave propagation before breaking does not seem so sensitive to small variations α, but the ratio h_{SPH}/dp has major influence on numerical model accuracy especially for large domains and very long simulations (Rota Roselli et al., 2018), the accuracy of the numerical simulation worsens at the breaking and in particular for post-breaking stages (Luo et al., 2021; Rota Roselli et al., 2019). For cases, like the ones here studied, where heavy wave breaking is induced by the presence of a shallow or very shallow foreshore, the flow after breaking has the characteristics of a bore. From a hydrodynamic point of view, a bore can be assumed similar

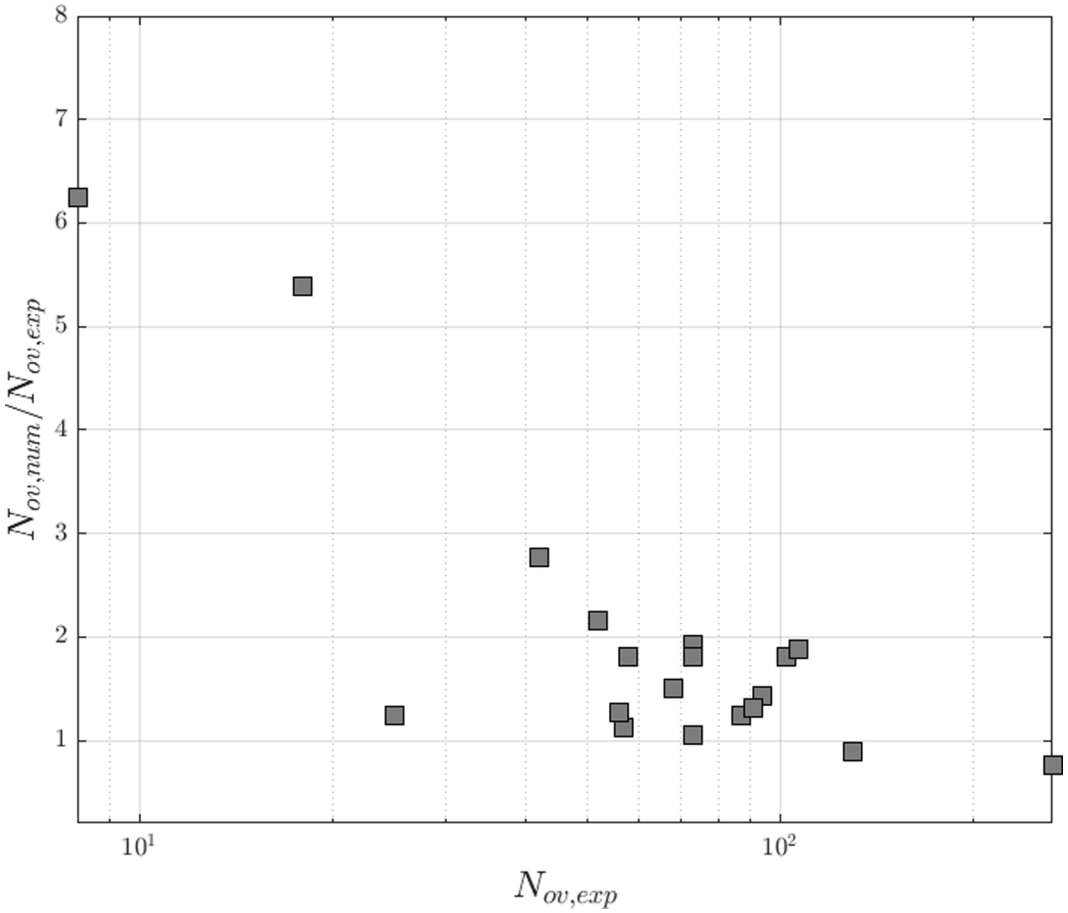

Fig. 20. Errors in number of overtopping waves.

to the tip of a dam break problem, where consolidated experience in SPH modelling shows that an accurate simulation of the velocity of the tip and the dam break water surface elevation is dependent on the correct choice of the artificial viscosity factor and numerical model resolution (Zeng and Shen, 2019). A few studies analyse the influence of the artificial viscosity factor on problems involving heavy wave breaking showing that varying the model resolution would require to vary the value of α to maintain accuracy (De Padova et al., 2014; Domínguez et al., 2019). Mokos et al. (2020) analysed the influence of viscosity term on the simulated overtopped water volume, concluding that viscous terms must be avoided if employed for simulations of waves without a kernel renormalisation term.

Actually, as also detailed in §3.1, the scale of the artificial viscosity factor α can be linked to the real fluid viscosity and the same simulated Reynold number can be expressed as function of α (Meringolo et al., 2019). The tuning of alpha is therefore related to the eddy structures created and solved in SPH. Higher values of α correspond to vertical structures of larger scale but less intensity. Meringolo et al. (2019) demonstrated that while using both artificial viscosity and a density diffusion scheme, that the whole dissipated energy stays the same while varying α, but the variation of α makes that the vorticity distributes at different scales. To this respect and for the test cases analyses in the present work, it is important not only to analyse the effect of the artificial viscosity on the numerical model performance, but also to take into proper account possible scale effects in the experimental modelling actually generated by an incorrect and unneglectable scaling of the viscous forces.

In the present simulation, considering the only used model resolution, a preliminary analysis of the influence of artificial viscosity on overtopping was required, showing that model performance increases using $\alpha = 0.015$, for $dp = 0.01$ m. The cumulative overtopping for the six test cases shown in Fig. 8 is compared for two values of α in Fig. 15, namely 0.015 and 0.01. It can be observed as overall the model performance increases for $\alpha = 0.015$, however the improvements are larger for those cases characterized by lower discharges. These cases are actually those with lower Reynolds numbers that required a correction of the wave measured discharge to compensate the scale effects.

If a much finer resolution is employed, e.g. for resolving the hydrodynamics of individual overtopping flows over the dike crest, it is recommended to further analyse the dependence of the results on the value of the artificial viscosity factor.

5.4. Long duration events

The accuracy and performance of a numerical wave model to reproduce long time series for large domains depends on the stability and robustness of the employed numerical scheme. A novel density diffusion scheme, along with the use of artificial viscosity and mDBC allowed attaining accurate results for wave overtopping prediction of wave trains of almost 1300 s. This duration, in model scale, corresponds to wave trains composed by 1000 waves, hence representative of real sea states employed for experimental modelling and design of coastal structures. Long wave trains are essential to get the statistics of the phenomena at stake: overtopping discharge has been proven to depend on the wave train duration (Romano et al., 2015; Williams et al., 2014). At the same time, infinite time domain realisations are possible for the same sea state: the influence of the generated time series is proven to increase for low overtopping discharges (namely lower than 1–5 l/s/m), leading to higher level of uncertainties when for low percentages of overtopping waves. Based on results of a NLSWE solver, Williams et al.

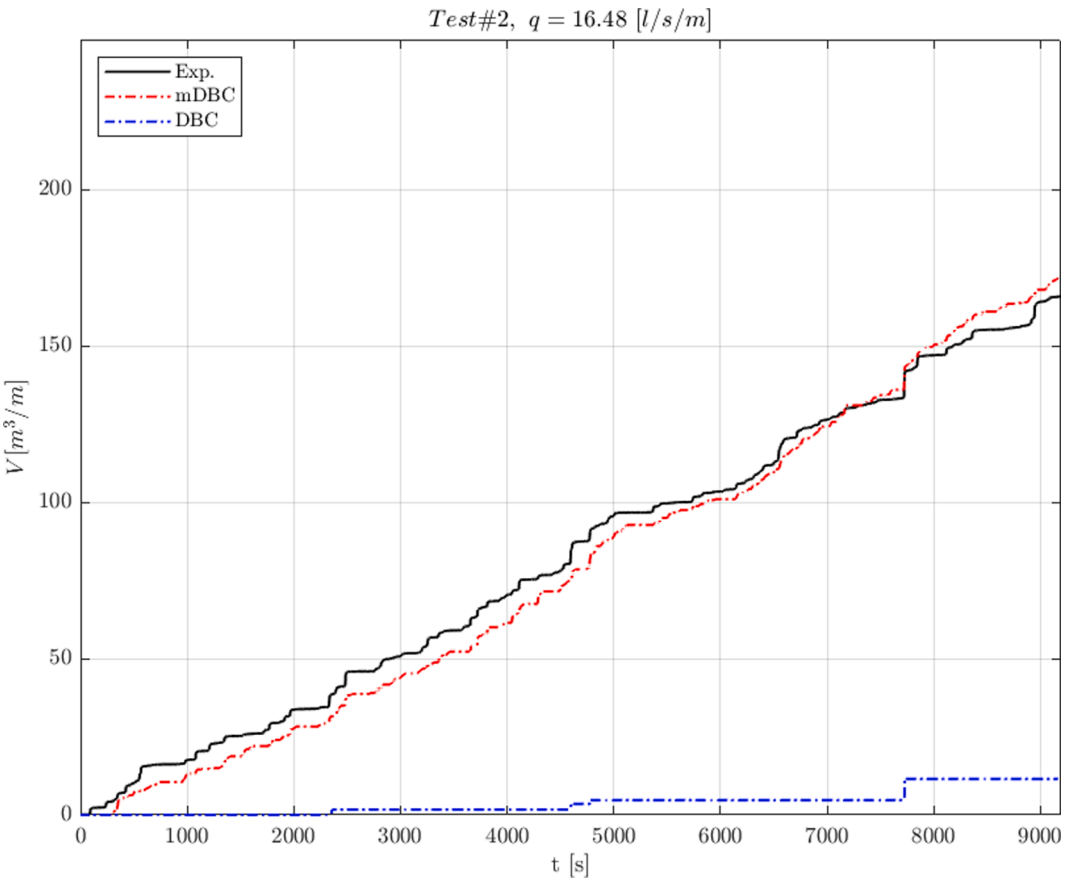

Fig. 21. Test case #2: comparison between mDBC and DBC setup of predicted cumulative overtopping volumes (results in prototype scale, 1:1).

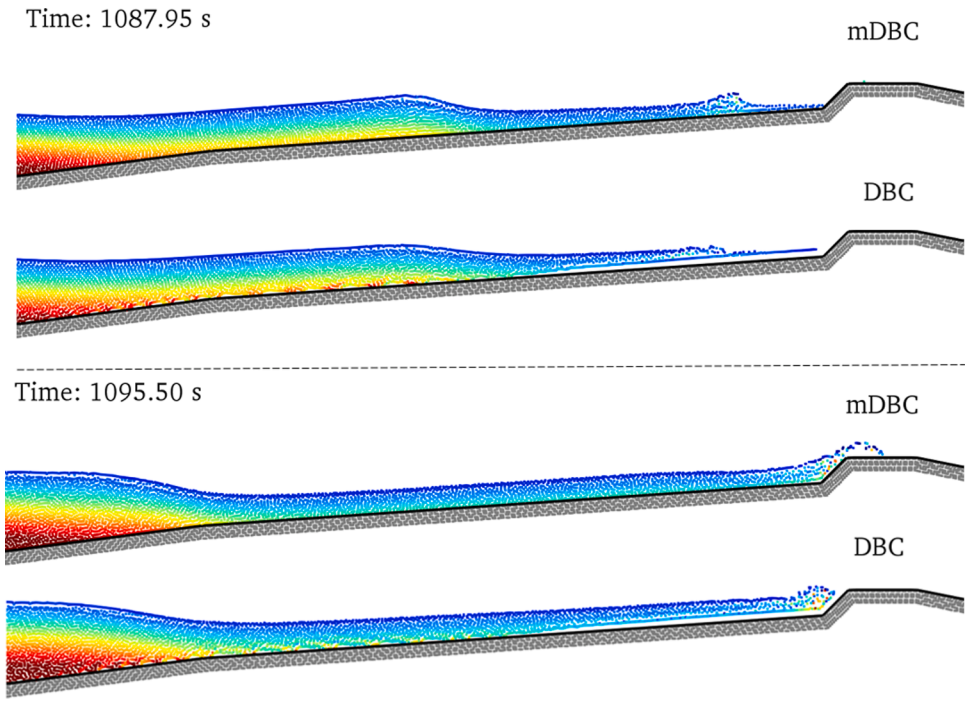

Fig. 22. Test case #2: snapshot of numerical model simulation at $t = 1087.95$ s and $t = 1095.50$ s for mDBC and DBC setup.

(2014) concluded that "*the numerical prediction of overtopping should be carried out using more than one numerical test starting from spectral offshore boundary conditions*". This conclusion, if extrapolated to mesh-less method and in particular to SPH-based model, lacking of variable resolution, supports the fact a trade-off must be attained between model accuracy and computational runtime, when SPH is employed for

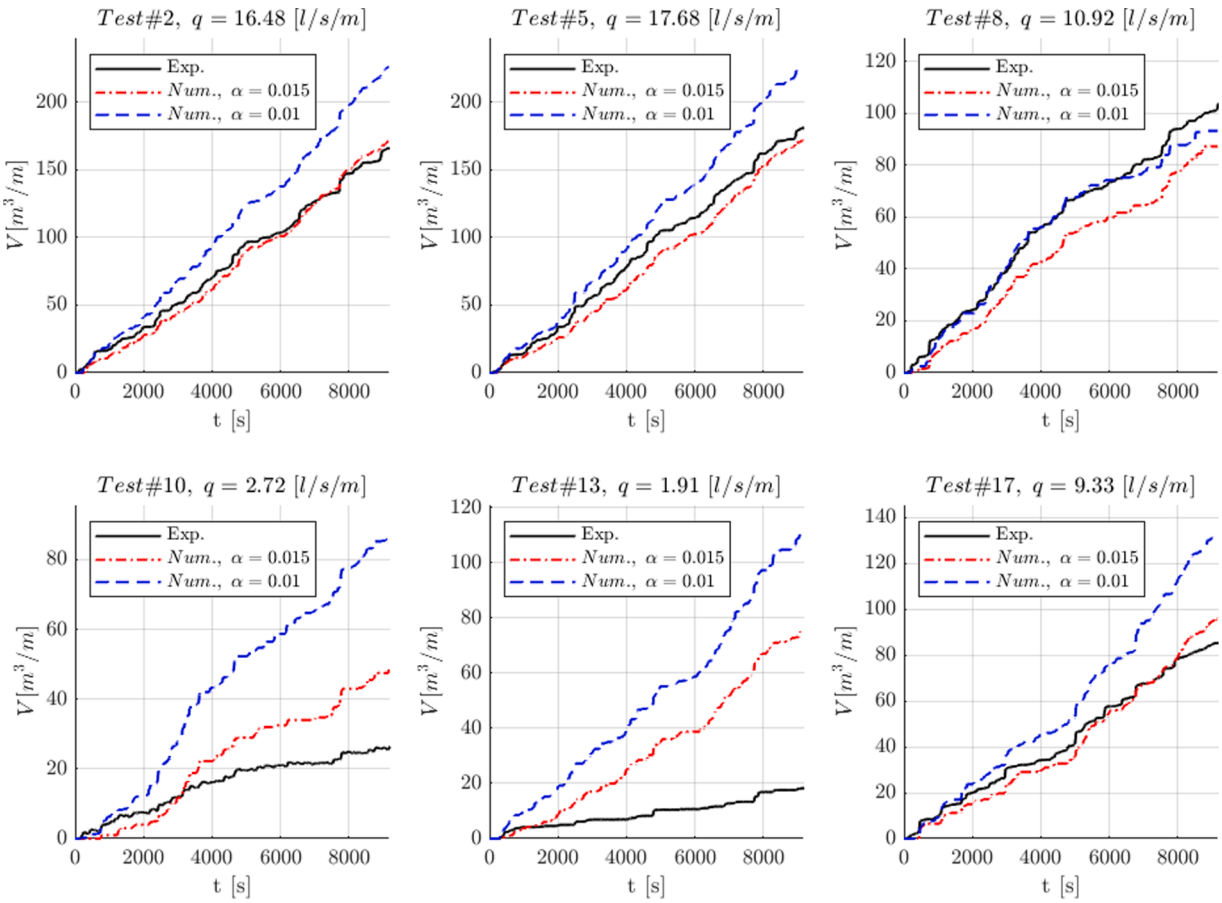

Fig. 23. Influence of the artificial viscosity factor on the predicted cumulative overtopping volumes for test cases #2, #5, #8, #10, #13 and #17. (results in prototype scale, 1:1).

assessment of random wave overtopping discharges. To this respect, model resolution, expressed by the initial inter-particle distance *dp* plays a major role for a such multi-scale problem. The resolution must be fine enough to achieve a *good* or *reasonable* model performance (see Table 3) at least for the modelling of the wave transformation all over the domain. At the same time, computational time must be limited to a few hours, to allow employing the model for several different overtopping scenarios. Even when finest resolutions would be used in order not only to measure mean discharges and volumes but also to properly resolve the hydrodynamics of individual overtopping flows, other discrepancies between numerical and experimental modelling would still lead to residual inaccuracies, such as:

- Modelling of viscous forces and surface tensions in the numerical model and presence of scale effects in the experimental models due to small model scales.
- Cross-waves and 3-D effects in the experimental campaign (e.g. wave front usually present some distortion, especially at breaking, mostly caused by the friction of the flume side walls and geometrical irregularities of the bottom in the third dimension, i.g. across the flume), which are not reproduced in a 2D model.
- Influence of water-air mixing in broken waves and overtopping flows, not represented in a single phase numerical model.
- Boundary treatment including slip and non-slip condition and boundary friction modelling.
- Uncertainties in the experimental measurement setup, especially when employed to measure flow velocity at small model scales. Non-intrusive or indirect measurements are employed (e.g. high-speed cameras, Bubble Image Velocimetry techniques), while in the numerical model a direct and easy measurement of any properties of the flow in any part of the domain can be performed.

6. Conclusions

The open-source DualSPHysics code has been used to model wave overtopping characterising dike-promenade coastal defence. DualSPHysics has been validated against data from 20 test cases carried out during an experimental campaign at the small-scale flume facility CIEMito, at UPC. Tests have been selected to cover a wide range of overtopping discharges and offshore wave steepnesses. The novelty of this work lies in the use of a new density diffusion scheme and the new modified Dynamic Boundary Conditions to simulate very long time series, corresponding to a train of random waves having a duration equal to 1000 waves. Cumulative overtopping volumes and mean discharges are calculated and compared with the experimental ones, showing a very good agreement and accuracy in terms of overtopping. Despite the initial relatively coarse resolution ($dp = 0.01$ m) due to computational time consumption, the model performance rates from *fair* to *very good*, based on rating and classification based on the index of agreement (Table 4). Accuracy was found related to the mean discharge value: lower the simulated discharge, larger the numerical model deviation for the same initial *dp*. Upscaling the overtopping discharge to real conditions, it is shown that overtopping predictions match experimental ones for discharge values larger than 4 l/s/m, while for lower discharges larger deviation is observed. Nevertheless, the differences are within the uncertainties of semi-empirical formulas for overtopping prediction. To our knowledge this is one of a few cases where very long simulations are performed (1000 waves = 1300 s in real time) providing stable and accurate results. Yet, further improvements such as variable resolution

might be beneficial to resolve the hydrodynamics of the individual flow properties, while keeping reasonable computational costs.

Funding

This research was funded by European Union's Horizon 2020 research and innovation programme under the Marie Sklodowska-Curie grant agreement No.: 792370.

Appendix A. Model parameter sensitivity

The test case #13 has been selected to carry out a sensitivity analysis based on the variation of the resolution, *dp*, and artificial viscosity factor. The choice of test #13 is justified by the fact that it is one of the cases with largest deviation between experimental and numerical model results. As already explained in §5.3, artificial viscosity plays a major role in problems characterized by wave breaking. Henceforth, for a complete overview of the model response to the variation of model resolution, the variation of the artificial viscosity factor must be considered. Six different values of α have been considered [0.01; 0.015; 0.02; 0.03; 0.05; 0.1] in combination with three values of initial inter-particle distance *dp* [0.002 m; 0.005 m; 0.01 m], resulting in 18 different cases. The results of two of these cases have been already shown previously, for $dp = 0.01$ and $\alpha = 0.01$ and 0.015, respectively.

First of all, the water surface elevation has been compared for different model resolutions. The comparison for different resolutions and a value of α equal to 0.01 is shown in Fig. A.1 for WG2, WG4 and WG7. The differences between resolutions appear negligible, a part from some peak overestimation while using the finest resolution ($dp = 0.002$ m).

The numerical time series of the cumulative overtopping volumes against the experimental ones are plotted in Fig. A.2. The reader must consider that this case is one of those that was affected by scale effects. The post-processing of the experimental data led to a calculation of a correction coefficient ≈ 1.7 for the average discharge. The same amplification factor has been applied to each individual overtopping volume. Doing that, a time series of experimental values but with scale effects corrected is derived. Although to adopt the correction coefficient from mean discharges for the overtopping time series is quite a strong assumption, a numerical model prediction could be considered accurate if close to the experimental corrected time series or anyway in between the corrected one and the original one.

In Fig. A.2, each plot corresponds to a different value of α. The line style of the numerical time series is different for each *dp* value, namely a solid line refers to $dp = 0.01$ m, a dashed line for $dp = 0.005$ m and a dot-dashed line for $dp = 0.002$ m. The first noticeable result is that, at least for all the values of *dp* employed, artificial viscosity factors equal to 0.05 and 0.1 cause too much dissipation leading to very small discharges or even no overtopping events.

In general, while α increases, the overtopping discharge, volumes and number of events decrease, as expected since an increase in viscosity leads to an increase of numerical dissipation. For a single value of α, while decreasing the value of *dp* there is not clear convergence of the numerical results to the experimental ones. For $\alpha = 0.01$ and $\alpha = 0.03$ it appears so, but different behaviour is noticed for $\alpha = 0.015$ and 0.02, where $dp = 0.005$ m leads to the largest deviations. In Fig. A.3, results for $\alpha = 0.05$ and $\alpha = 0.1$ were discarded, in order to show a zoomed in view of the cases employing lower values of α. The most accurate prediction is achieved for $\alpha = 0.03$ and $dp = 0.002$ m, while even for $dp = 0.005$ m, there is a good agreement with the experimental results with correction of scale effects.

The combined influence of α and *dp* is demonstrated, as expected looking at the existing literature (De Padova et al., 2014; Rota Roselli et al., 2019). However, a deeper study on the parametrization of the model response to α and *dp* is out of the scope of the present work.

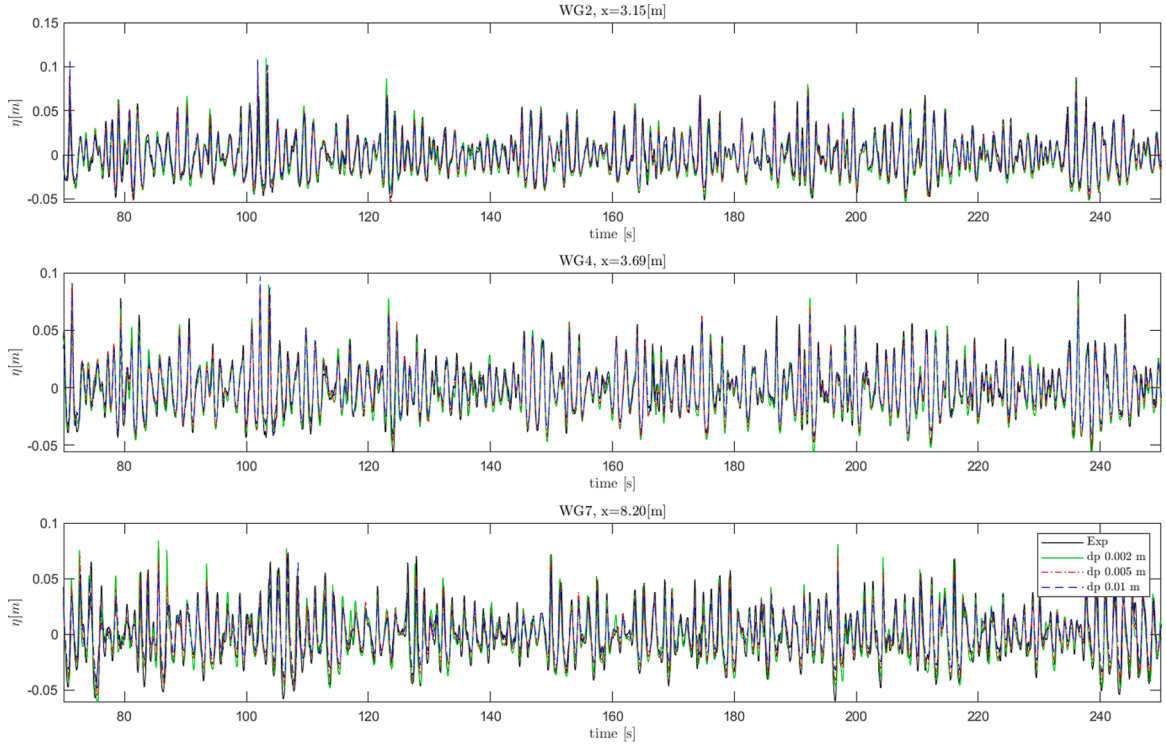

Fig. A.1. Comparison of the time series at WG2, WG4, and WG7 location for test #13 for a 180 s time window (results shown in model scale, 1:50) for different model resolutions.

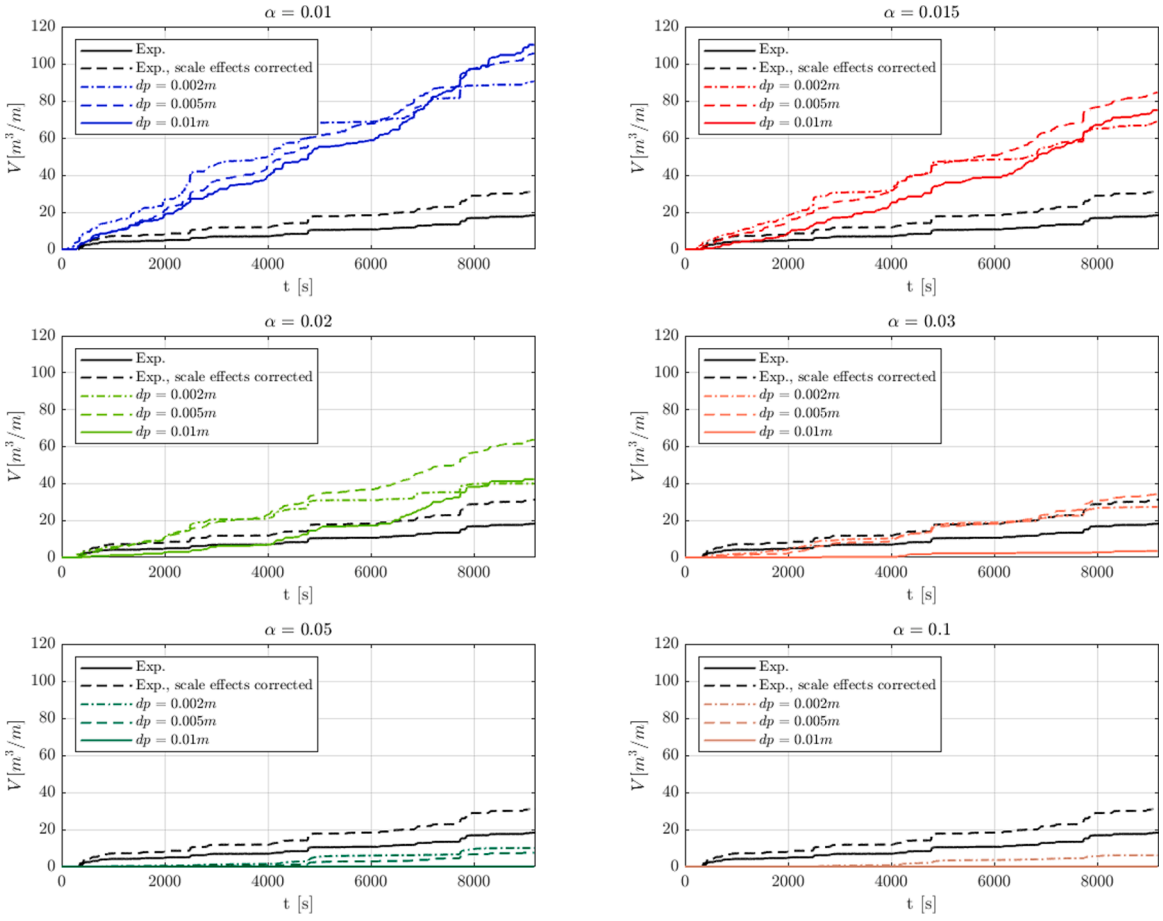

Fig. A.2. Influence of the artificial viscosity factor and model resolution on the predicted cumulative overtopping volumes for test case #13. (results in prototype scale, 1:1).

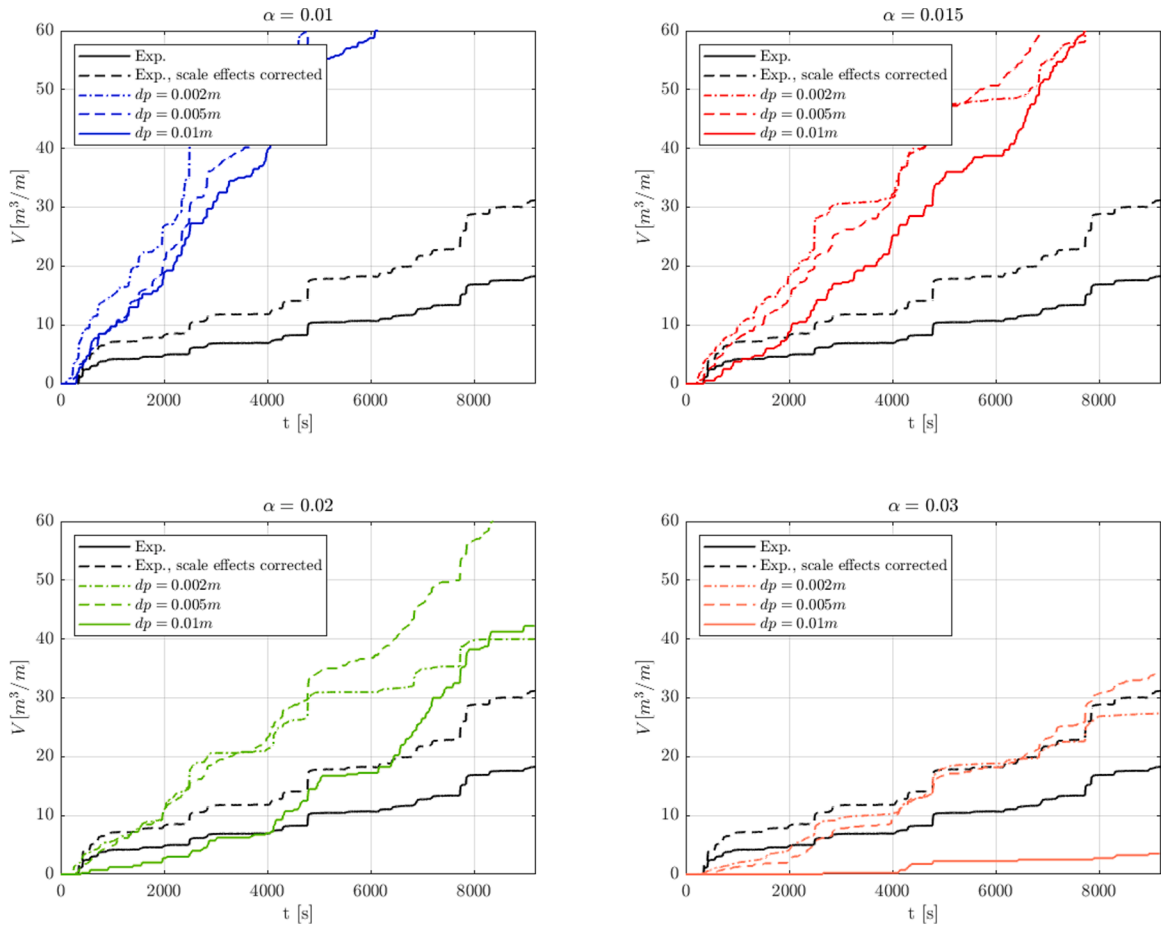

Fig. A.3. Influence of the artificial viscosity factor and model resolution on the predicted cumulative overtopping volumes for test case #13: zoomed in view of results for α equal to 0.01, 0.015, 0.02 and 0.03 (results in prototype scale, 1:1).

CRediT authorship contribution statement

Corrado Altomare: Conceptualization, Methodology, Data curation, Investigation, Funding acquisition, Writing – original draft, Validation, Project administration. **Xavi Gironella:** Funding acquisition, Investigation, Supervision. **Alejandro J.C. Crespo:** Writing – review & editing, Methodology, Software.

Declaration of Competing Interest

The authors declare that they have no known competing financial interests or personal relationships that could have appeared to influence the work reported in this paper.

References

Akbari, H., 2017. Simulation of wave overtopping using an improved SPH method. Coast. Eng. 126, 51–68 https://doi.org/10.1016/j.coastaleng.2017.04.010.

Altomare, C., 2021. DURCWAVE - CIEMito. https://doi.org/10.5821/DATA-2117-342397-1.

Altomare, C., Crespo, A.J.C., Domínguez, J.M., Gómez-Gesteira, M., Suzuki, T., Verwaest, T., 2015a. Applicability of smoothed particle hydrodynamics for estimation of sea wave impact on coastal structures. Coast. Eng. 96, 1–12 https://doi.org/10.1016/j.coastaleng.2014.11.001.

Altomare, C., Crespo, A.J.C., Rogers, B.D., Domínguez, J.M., Gironella, X., Gómez-Gesteira, M., 2014. Numerical modelling of armour block sea breakwater with Smoothed Particle Hydrodynamics. Comput. Struct. Comput. Struct. 130, 34–45 https://doi.org/10.1016/j.compstruc.2013.10.011.

Altomare, C., Domínguez, J.M., Crespo, A.J.C., Suzuki, T., Caceres, I., Gómez-Gesteira, M., 2015b. Hybridization of the wave propagation model SWASH and the meshfree particle method SPH for real coastal applications. Coast. Eng. J. https://doi.org/10.1142/S0578563415500242.

Altomare, C., Domínguez, J.M., Crespo, A.J.C., González-Cao, J., Suzuki, T., Gómez-Gesteira, M., Troch, P., 2017. Long-crested wave generation and absorption for SPH-based DualSPHysics model. Coast. Eng. 127 https://doi.org/10.1016/j.coastaleng.2017.06.004.

Altomare, C., Gironella, X., Suzuki, T., Viccione, G., Saponieri, A., 2020. Overtopping Metrics and Coastal Safety: A Case of Study from the Catalan Coast. J. Mar. Sci. Eng. 8, 556. https://doi.org/10.3390/jmse8080556.

Altomare, C., Suzuki, T., Chen, X., Verwaest, T., Kortenhaus, A., 2016. Wave overtopping of sea dikes with very shallow foreshores. Coast. Eng. 116, 236–257. https://doi.org/10.1016/j.coastaleng.2016.07.002.

Altomare, C., Tagliafierro, B., Dominguez, J.M., Suzuki, T., Viccione, G., 2018a. Improved relaxation zone method in SPH-based model for coastal engineering applications. Appl. Ocean Res. 81, 15–33 https://doi.org/10.1016/J.APOR.2018.09.013.

Altomare, Corrado, Tagliafierro, B., Suzuki, T., Dominguez, J.M., Crespo, A.J.C., Briganti, R., 2018b. Relaxation zone method in SPH-based model applied to wave-structure interaction. In: International Ocean and Polar Engineering Conference. Sapporo. , pp. 627-634.

Booij, N., Holthuijsen, L.H., Ris, R.C., 1996. The "Swan" Wave Model for Shallow Water. Coastal Engineering 668–676. https://doi.org/10.1061/9780784402429.053.

Crespo, A.J.C., Altomare, C., Domínguez, J.M., González-Cao, J., Gómez-Gesteira, M., 2017. Towards simulating floating offshore oscillating water column converters with Smoothed Particle Hydrodynamics. Coast. Eng. 126 https://doi.org/10.1016/j.coastaleng.2017.05.001.

Crespo, A.J.C., Gómez-Gesteira, M., Dalrymple, R.A., 2007. Boundary conditions generated by dynamic particles in SPH methods. Comput. Mater. Continua. 5, 173–184 https://doi.org/10.3970/cmc.2007.005.173.

Dang, B.-L., Nguyen-Xuan, H., Abdel Wahab, M., 2021. Numerical study on wave forces and overtopping over various seawall structures using advanced SPH-based method. Eng. Struct. 226, 111349 https://doi.org/10.1016/j.engstruct.2020.111349.

De Finis, S., Romano, A., Bellotti, G., 2020. Numerical and laboratory analysis of post-overtopping wave impacts on a storm wall for a dike-promenade structure. Coastal Engineering 155. https://doi.org/10.1016/j.coastaleng.2019.103598.

De Padova, D., Dalrymple, R.A., Mossa, M., 2014. Analysis of the artificial viscosity in the smoothed particle hydrodynamics modelling of regular waves. J. Hydraul. Res. 52, 836–848 https://doi.org/10.1080/00221686.2014.932853.

Domínguez, J.M., Altomare, C., Gonzalez-Cao, J., Lomonaco, P., 2019. Towards a more complete tool for coastal engineering: solitary wave generation, propagation and

breaking in an SPH-based model. Coast. Eng. J. 61, 15–40 https://doi.org/10.1080/21664250.2018.1560682.
Domínguez, J.M., Fourtakas, G., Altomare, C., Canelas, R.B., Tafuni, A., García-Feal, O., Martínez-Estévez, I., Mokos, A., Vacondio, R., Crespo, A.J.C., Rogers, B.D., Stansby, P.K., Gómez-Gesteira, M., 2021. DualSPHysics: from fluid dynamics to multiphysics problems. Comput. Part. Mech. https://doi.org/10.1007/s40571-021-00404-2.
English, A., Domínguez, J.M., Vacondio, R., Crespo, A.J.C., Stansby, P.K., Lind, S.J., Chiapponi, L., Gómez-Gesteira, M., 2021. Modified dynamic boundary conditions (mDBC) for general-purpose smoothed particle hydrodynamics (SPH): application to tank sloshing, dam break and fish pass problems. Comput. Part. Mech. https://doi.org/10.1007/s40571-021-00403-3.
EurOtop, 2018. Manual on wave overtopping of sea defences and related structures. An overtopping manual largely based on European research, but for worldwide application. Van der Meer, J.W., Allsop, N.W.H., Bruce, T., De Rouck, J., Kortenhaus, A., Pullen, T., Schüttrumpf.
Fourtakas, G., Dominguez, J.M., Vacondio, R., Rogers, B.D., 2019. Local uniform stencil (LUST) boundary condition for arbitrary 3-D boundaries in parallel smoothed particle hydrodynamics (SPH) models. Comput. Fluids 190, 346–361 https://doi.org/https://doi.org/10.1016/j.compfluid.2019.06.009.
Gallien, T.W., Sanders, B.F., Flick, R.E., 2014. Urban coastal flood prediction: integrating wave overtopping, flood defenses and drainage. Coast. Eng. 91, 18–28 https://doi.org/10.1016/j.coastaleng.2014.04.007.
Goda, Y., 2009. Derivation of unified wave overtopping formulas for seawalls with smooth, impermeable surfaces based on selected CLASH datasets. Coast. Eng. 56, 385–399 https://doi.org/10.1016/j.coastaleng.2008.09.007.
González-Cao, J., Altomare, C., Crespo, A.J.C., Domínguez, J.M., Gómez-Gesteira, M., Kisacik, D., 2019. On the accuracy of DualSPHysics to assess violent collisions with coastal structures. Comput. Fluids 179 https://doi.org/10.1016/j.compfluid.2018.11.021.
Gotoh, H., Khayyer, A., 2018. On the state-of-the-art of particle methods for coastal and ocean engineering. Coast. Eng. J. 0, 1–25 https://doi.org/10.1080/21664250.2018.1436243.
Gruwez, V., Altomare, C., Suzuki, T., Streicher, M., Cappietti, L., Kortenhaus, A., Troch, P., 2020a. Validation of RANS modelling for wave interactions with sea dikes on shallow foreshores using a large-scale experimental dataset. J. Mar. Sci. Eng. 8, 650 https://doi.org/10.3390/jmse8090650.
Gruwez, V., Altomare, C., Suzuki, T., Streicher, M., Cappietti, L., Kortenhaus, A., Troch, P., 2020b. An Inter-model comparison for wave interactions with sea dikes on shallow foreshores. J. Mar. Sci. Eng. 8, 985 https://doi.org/10.3390/jmse8120985.
Heller, V., 2011. Scale effects in physical hydraulic engineering models. J. Hydraul. Res. 49, 293–306 https://doi.org/10.1080/00221686.2011.578914.
Hofland, B., Chen, X., Altomare, C., Oosterlo, P., 2017. Prediction formula for the spectral wave period Tm-1,0 on mildly sloping shallow foreshores 123, 21-28. https://doi.org/10.1016/j.coastaleng.2017.02.005.
Khayyer, A., Gotoh, H., Shao, S.D., 2008. Corrected incompressible SPH method for accurate water-surface tracking in breaking waves. Coast. Eng. 55, 236–250 https://doi.org/10.1016/j.coastaleng.2007.10.001.
Lashley, C.H., Zanuttigh, B., Bricker, J.D., van der Meer, J., Altomare, C., Suzuki, T., Roeber, V., Oosterlo, P., 2020. Benchmarking of numerical models for wave overtopping at dikes with shallow mildly sloping foreshores: accuracy versus speed. Environ. Model. Softw. 130, 104740 https://doi.org/https://doi.org/10.1016/j.envsoft.2020.104740.
Losada, I.J., Lara, J.L., Guanche, R., Gonzalez-Ondina, J.M., 2008. Numerical analysis of wave overtopping of rubble mound breakwaters. Coast. Eng. 55, 47–62 https://doi.org/10.1016/j.coastaleng.2007.06.003.
Lowe, R.J., Buckley, M.L., Altomare, C., Rijnsdorp, D.P., Yao, Y., Suzuki, T., Bricker, J., 2019. Numerical simulations of surf zone wave dynamics using smoothed particle hydrodynamics. Ocean Model., 101481 https://doi.org/10.1016/J.OCEMOD.2019.101481.
Luo, M., Khayyer, A., Lin, P., 2021. Particle methods in ocean and coastal engineering. Appl. Ocean Res. 114, 102734 https://doi.org/10.1016/j.apor.2021.102734.
Lynett, P., 2006. Wave breaking velocity effects in depth-integrated models. Coastal Engineering 53 (4), 325–333. https://doi.org/10.1016/j.coastaleng.2005.10.020.
Mares-Nasarre, P., Argente, G., Gómez-Martín, M.E., Medina, J.R., 2019. Overtopping layer thickness and overtopping flow velocity on mound breakwaters. Coast. Eng. 154 https://doi.org/10.1016/j.coastaleng.2019.103561.
Meringolo, D.D., Marrone, S., Colagrossi, A., Liu, Y., 2019. A dynamic δ-SPH model: how to get rid of diffusive parameter tuning. Comput. Fluids 179, 334–355 https://doi.org/10.1016/j.compfluid.2018.11.012.
Mokos, A., Carmigniani, R., Leroy, A., Violeau, D., 2020. Simulating wave overtopping on a complex coastal structure using SPH. J. Appl. Water Eng. Res. 8, 55–65 https://doi.org/10.1080/23249676.2020.1719221.
Molteni, D., Colagrossi, A., 2009. A simple procedure to improve the pressure evaluation in hydrodynamic context using the SPH. Comput. Phys. Commun. 180, 861–872 https://doi.org/10.1016/j.cpc.2008.12.004.
Monaghan, J.K.A., 1999. Solitary Waves on a Cretan Beach. J. Waterway, Port, Coast., Ocean Eng. 125, 145–155 https://doi.org/10.1061/(ASCE)0733-950X(1999)125:3(145).
Monaghan, J.J., 2005. Smoothed particle hydrodynamics. Rep. Prog. Phys. 68, 1703–1759 https://doi.org/10.1088/0034-4885/68/8/R01.
Monaghan, J.J., 1994. Simulating free surface flows with SPH. J. Comput. Phys. 110, 399–406 https://doi.org/10.1006/jcph.1994.1034.
Monaghan, J.J., 1992. Smoothed Particle Hydrodynamics. Ann. Rev.Astron. Astrophys. 30, 543–574 https://doi.org/10.1146/annurev.aa.30.090192.002551.
Oger, G., Le Touzé, D., Ducrozet, G., Candelier, J., Guilcher, P.-M., 2014. A coupled SPH-spectral method for the simulation of wave train impacts on a FPSO. https://doi.org/10.1115/OMAE2014-24679.
Romano, A., Bellotti, G., Briganti, R., Franco, L., 2015. Uncertainties in the physical modelling of the wave overtopping over a rubble mound breakwater: the role of the seeding number and of the test duration. Coast. Eng. 103, 15–21 https://doi.org/10.1016/j.coastaleng.2015.05.005.
Rota Roselli, R.A., Vernengo, G., Altomare, C., Brizzolara, S., Bonfiglio, L., Guercio, R., 2018. Ensuring numerical stability of wave propagation by tuning model parameters using genetic algorithms and response surface methods. Environ. Model. Softw. 103 https://doi.org/10.1016/j.envsoft.2018.02.003.
Rota Roselli, R.A., Vernengo, G., Brizzolara, S., Guercio, R., 2019. SPH simulation of periodic wave breaking in the surf zone - A detailed fluid dynamic validation. Ocean Eng. 176, 20–30 https://doi.org/10.1016/J.OCEANENG.2019.02.013.
Sandoval, C, Bruce, T., 2017. Wave overtopping hazard to pedestrians: video evidence from real accidents. In: Coasts, Marine Structures and Breakwaters 2017. ICE Publishing, pp. 501–512 https://doi.org/10.1680/cmsb.63174.0501.
Schüttrumpf, H., Oumeraci, H., 2005. Scale and model effects in crest level design. In: Proc. 2nd Coastal Symposium. Höfn. Iceland., pp. 1–12.
Shao, S., 2006. Incompressible SPH simulation of wave breaking and overtopping with turbulence modelling 597–621.
Shao, S., Ji, C., Graham, D.I., Reeve, D.E., James, P.W., Chadwick, A.J., 2006. Simulation of wave overtopping by an incompressible SPH model. Coast. Eng. 53, 723–735 https://doi.org/10.1016/j.coastaleng.2006.02.005.
Spreng, F., Vacondio, R., Eberhard, P., Williams, J.R., 2020. An advanced study on discretization-error-based adaptivity in Smoothed Particle Hydrodynamics. Comput. Fluids 198, 104388 https://doi.org/10.1016/j.compfluid.2019.104388.
St-germain, P., Nistor, I., Asce, M., Townsend, R., Shibayama, T., 2014. Smoothed-particle hydrodynamics numerical modeling of structures impacted by Tsunami Bores 1, 66–81. https://doi.org/10.1061/(ASCE)WW.1943-5460.0000225.
Stansby, P.K., Lind, S.J., Rogers, B.D., 2020. Review of smoothed particle hydrodynamics: towards converged Lagrangian flow modelling. https://doi.org/10.1098/rspa.2019.0801.
Sutherland, J., Walstra, D.J.R., Chesher, T.J., van Rijn, L.C., Southgate, H.N., 2004. Evaluation of coastal area modelling systems at an estuary mouth. Coast. Eng. 51, 119–142 https://doi.org/10.1016/j.coastaleng.2003.12.003.
Tafuni, A., Domínguez, J.M., Vacondio, R., Crespo, A.J.C., 2018. A versatile algorithm for the treatment of open boundary conditions in Smoothed particle hydrodynamics GPU models. Comput. Methods Appl. Mech. Eng. 342, 604–624 https://doi.org/https://doi.org/10.1016/j.cma.2018.08.004.
Vacondio, R., Altomare, C., De Leffe, M., Hu, X., Le Touzé, D., Lind, S., Marongiu, J.-C., Marrone, S., Rogers, B.D., Souto-Iglesias, A., 2021. Grand challenges for Smoothed Particle Hydrodynamics numerical schemes. Comput. Part. Mech. 8, 575–588 https://doi.org/10.1007/s40571-020-00354-1.
Verbrugghe, T., Domínguez, J.M., Altomare, C., Tafuni, A., Vacondio, R., Troch, P., Kortenhaus, A., 2019. Non-linear wave generation and absorption using open boundaries within DualSPHysics. Comput. Phys. Commun. 240 https://doi.org/10.1016/j.cpc.2019.02.003.
Verbrugghe, T., Domínguez, J.M., Crespo, A.J.C., Altomare, C., Stratigaki, V., Troch, P., Kortenhaus, A., 2018. Coupling methodology for smoothed particle hydrodynamics modelling of non-linear wave-structure interactions. Coast. Eng. 138, 184–198 https://doi.org/10.1016/j.coastaleng.2018.04.021.
Violeau, D., 2012. Fluid Mechanics and the SPH Method: theory and Applications, Fluid Mechanics and the SPH Method: theory and Applications. https://doi.org/10.1093/acprof:oso/9780199655526.001.0001.
Wen, H., Ren, B., Dong, P., Wang, Y., 2016. A SPH numerical wave basin for modeling wave-structure interactions. Appl. Ocean Res. 59, 366–377 https://doi.org/10.1016/j.apor.2016.06.012.
Wen, H., Ren, B., Wang, G., 2018. 3D SPH porous flow model for wave interaction with permeable structures. Appl. Ocean Res. 75, 223–233 https://doi.org/10.1016/J.APOR.2018.04.003.
Wendland, H., 1995. Piecewise polynomial, positive definite and compactly supported radial functions of minimal degree. Adv. Comput. Math. 4, 389–396 https://doi.org/10.1007/BF02123482.
Williams, H.E., Briganti, R., Pullen, T., 2014. The role of offshore boundary conditions in the uncertainty of numerical prediction of wave overtopping using non-linear shallow water equations. Coast. Eng. 89, 30–44 https://doi.org/10.1016/j.coastaleng.2014.03.003.
Willmott, C.J., Robeson, S.M., Matsuura, K., 2012. A refined index of model performance. Int. J. Climatol. 32, 2088–2094 https://doi.org/https://doi.org/10.1002/joc.2419.
You, Y., Khayyer, A., Zheng, X., Gotoh, H., Ma, Q., 2021. Enhancement of δ-SPH for ocean engineering applications through incorporation of a background mesh scheme. Appl. Ocean Res. 102508https://doi.org/10.1016/j.apor.2020.102508.
Yuhi, M., Mase, H., Kim, S., Umeda, S., Altomare, C., 2021. Refinement of integrated formula of wave overtopping and runup modeling. Ocean Eng. 220, 108350 https://doi.org/10.1016/j.oceaneng.2020.108350.
Zeng, J., Shen, J.L.H., 2019. A parametric study of dam break flow feature over a dry bed usinh SPH modelling. In: Proceedings of the 10th International Conference on Asian and Pacific Coasts, 2019, Hanoi, Vietnam.
Zijlema, M., Stelling, G., Smit, P., 2011. SWASH: An operational public domain code for simulating wave fields and rapidly varied flows in coastal waters. Coastal Engineering 58 (10), 992–1012. https://doi.org/10.1016/j.coastaleng.2011.05.015.